Hydrogen-enhanced intergranular failure of sulfur-doped nickel grain boundary: In situ electrochemical micro-cantilever bending vs. DFT

Tarlan Hajilou, Iman Taji, Frédéric Christien, Shuang He, Daniel Scheiber, Werner Ecker, Reinhard Pippan, Vsevolod I. Razumovskiy, Afrooz Barnoush

Hydrogen-enhanced intergranular failure of sulfur-doped nickel grain boundary: In situ electrochemical micro-cantilever bending vs. DFT

Tarlan Hajilou[a,*], Iman Taji[a], Frederic Christien[b], Shuang He[c,d], Daniel Scheiber[c], Werner Ecker[c], Reinhard Pippan[e], Vsevolod I. Razumovskiy[c], Afrooz Barnoush[a]

[a]*Department of Engineering Design and Materials, Norwegian University of Science and Technology, No. 7491 Trondheim, Norway*
[b]*Mines Saint-Etienne, Univ Lyon, CNRS, UMR 5307 LGF, Centre SMS, F-42023 Saint-Etienne, France*
[c]*Materials Center Leoben Forschung GmbH, Roseggerstraße 12, 8700 Leoben, Austria*
[d]*Department Materials Science, Montanuniversität Leoben, Jahnstraße 12, 8700 Leoben, Austria*
[e]*Erich Schmid Institute of Materials Science, Austrian Academy of Sciences, Jahnstraße 12, 8700 Leoben, Austria*

Abstract

Intergranular failure of nickel (Ni) single grain boundaries (GBs) owing to the segregation of sulfur (S), hydrogen (H), and their co-segregation has been investigated by employing micro-cantilever bending tests and density functional theory (DFT) calculations. A pure Ni GB shows completely plastic behavior with no fracture observed in the experiments. Electrochemical H-charging of the sample with no S present in the GB leads to a crack formed at the notch tip, which propagates by means of the mixed plastic–brittle fracture mode. Cantilever testing of the H-charged GB with S results in a clear brittle fracture of the GB. The co-segregation of S and H shifts the sudden drop in the load–displacement curves to smaller values of displacement. This is explained by the combined effect of these elements on the work of separation of the selected GB leading to severely decreased GB cohesion.

Keywords: Hydrogen embrittlement, Nickel, Sulfur segregation, Intergranular cracking, Density functional theory, Micro-cantilever

1. Introduction

Grain boundaries (GBs) are known as a common defect in metals and their alloys. As they possess higher energy compared with the bulk crystal, GBs are preferential sites for impurities to segregate. This segregation process is thermodynamically favorable if it reduces the total energy of the system. Depending on the segregation energy difference between the GB and free surface formed during fracture, segregated elements in the GB can be evaluated in terms of their influence on the GB embrittlement within the framework of the Rice–Wang theory of brittle fracture [1–3]. Fracture mode transition can be occurred due to (i) segregated embrittling metalloid impurities, hydrogen or alloying elements, (ii) precipitation formation, (iii) embrittling environmental species such as hydrogen adsorption to the GB [4]. Intergranular (IG) fracture is one of the most dangerous technical failures in metals and alloys which proceeds quickly owing to the interconnected network of the GBs. This type of failure is usually hard to detect prior to final rupture. The focus of this study is on nickel (Ni), one of the basic engineering materials, which has a face-centered cubic (FCC) crystal structure. Owing to the greater number of slip systems available in this structure, it is intrinsically ductile [5]. However, IG fracture of this metal can occur even at room temperature; this is usually associated with GB segregation of atoms of impurities [6, 7].

Various elements can segregate to Ni GBs. Comparing the embrittling effect of the different solute elements such as Sn, Sb, P, and S to the Ni GB, it was found that S was one of the most detrimental GB segregating elements owing to its high segregation potency and its major effect on the mechanical properties of the interfaces [8–10]. Sulfur (S) segregation to GBs in Ni is reported to convert the fracture mode of the material to IG failure by changing the local

*Corresponding author
Email address: tarlan.hajilou@ntnu.no (Tarlan Hajilou)

cohesive strength of the GB [5]. Atomic hydrogen (H) is another detrimental element that can be introduced into the material throughout the manufacturing process or can be adsorbed under service conditions such as exposure to cathodic protection, corrosion processes, or environments containing H gas. The embrittling effect of H on Ni and Ni alloys, and the correlation between the solute H concentration and the fracture mode transition have been studied extensively [11–13] which concluded with some proposed models to explain the metal- H interaction. Some of these mechanisms such as hydrogen-enhanced decohesion (HEDE) [14] is put forward based on the H effect on the cohesive strength weakening by dilatation of the atomic lattice bonding [15]. Since the hydrogen induced decohesion (HID) mechanism does not consider the plastic interaction of the H with dislocations, other mechanisms such as adsorption-induced dislocation emission (AIDE) and hydrogen-enhanced localized plasticity (HELP) were taken into account. Based on AIDE mechanism weakening of the interatomic bonds due to adsorbed H results in the dislocation emission from the crack tip which led to void nucleation and their coalescence ahead of the crack [4]. Effect of absorbed H on lattice dislocations, however, is considered in the HELP mechanism. This mechanism suggested the increased mobility of the dislocations motion and their tendency to pack closer together in the presence of H [16]. Almost all mechanisms are agreed on the role of H on dislocation nucleation enhancement which is explained by defectant theory [17], based upon thermodynamic consideration. This model suggests that the dislocation formation energy is reduced by H segregation to the dislocations. Beyond this step, usually a combination of the embrittling mechanisms are favored to explain the nano- micro scale phenomena behind the observed degradational effect in the presence of H. As an example, IG cracking of Ni in the presence of H is explained by HELP mediated HEDE model [18]. Plasticity enhancement by H increases the GB stress level. In addition, transport of H by dislocations to the GBs increases the GB H concentration and H accumulation in the GB would facilitate the GB interatomic debonding. Other possible mechanisms are also proposed in the literature [19]. Despite the discrepancies on the involved embrittlement mechanism, there is agreement in the literature on fracture mode transition to IG fracture by increasing the H fugacity in the material [11]. Up to now, most IG failure studies investigating the effect of segregated impurities such as H or S or their co-segregation on the mechanical properties of the alloy have been confined to polycrystalline materials. Diversity in the GB type and heterogeneity of the segregated element concentration in each GB results in different critical S or H concentration amounts that can induce IG cracking [11, 20]. Therefore, using polycrystalline materials, it is difficult to find a direct relationship between a selected GB type and segregation parameters and the mechanical response of that specific GB. However, a few studies can be found that have investigated a single GB. Vehoff et al. examined the effect of S and H on the GB embrittlement by growing a bi-crystal [21]. However, this approach to test a specific GB is quite difficult and also suffers from a lack of reproducibility.

Following the introduction of focused ion beam (FIB) scanning electron microscopy (SEM) technology, nowadays it is possible to make a series of identical micrometer-sized specimens in favorable positions on the material. The micro-cantilever bending test, which has drawn a lot of attention since its first use in 2005 [22], is an interesting method to explore the micro-mechanical variation of materials [23]. Putting a specific GB in the micro-cantilever makes it more convenient to study the segregation and environmental parameters on the mechanical behavior of the GB [24, 25]. Combining micro-milling with an electron back-scattered diffraction (EBSD) method enables us to select a favorable GB and test a series of identical cantilevers under different testing conditions. In addition, by confining the testing size to a micrometer scale and considering a specific GB, it is possible to compare the results with atomistic calculations, which can provide a fundamental understanding of the GB segregation and quantify the segregation-induced changes in GB cohesion. One of the prominent examples is the simulation of HEDE of GB in Ni [9, 26–29], which has shown that atomic H tended to segregate to the Ni GB and demonstrated the GB embrittling effect. Moreover, the synergistic effect between segregated impurities has drawn attention to the investigation of solute co-segregation at GBs, such as H–carbide co-segregation[30, 31], H–Cr co-segregation in α-Fe GB [32, 33], C–O co-segregation in α-Ti GB [34], C, B, O, Fe, and Hf co-segregation in Mo GB [35], or H–C and H–Mo co-segregation in Ni GB [29]. Although S is known to segregate to Ni GBs and decrease GB cohesion [10, 36–39], the H–S interaction and its co-segregation effect as well as the kinetics of H–S segregation in Ni GB have not been studied sufficiently at the atomic level.

In this study, micro-mechanical testing is combined with atomistic calculations to study the co-segregation effect of S and H in selected GBs. Selected GBs are tested with the micro-cantilever method to investigate the interaction of segregated impurities in GBs and their effect on the mechanical properties. From the computational side, this study applies density functional theory (DFT) to investigate the fundamentals of segregation and co-segregation of H with S in Ni and its effect on the GB cohesive strength using the Rice-Thomson-Wang theory of interface embrittlement [3, 40].With this approach, the focus is on the HEDE mechanism of H embrittlement (HE), which is the dominant

mechanism at high H concentrations [15]. Furthermore, the kinetics of H and S segregation to a Ni GB are investigated using our calculated segregation energies DFT and the McLean isotherm [1, 41–43]. The results of this study can be used to strengthen Ni and its alloys via GB engineering against environmental conditions.

2. Method

2.1. Materials and characterization

Two types of Ni samples were used in this study: (i) a pure Ni sample; and (ii) a S-doped Ni sample. The polycrystalline high-purity Ni sample (99.99 %) was produced by the zone refining process. Disk-shaped samples with a diameter of 12 mm and thickness of 4 mm were annealed in vacuum at 1250 °C for 72 h followed by furnace cooling as the final heat treatment step. The annealing process lead to grain growth with an average size of ~2 mm and GBs perpendicular to the surface of the sample [44]. The S-doped sample contains 5.4 wt ppm of S in solid solution condition measured by a glow discharge mass spectroscopy technique. Following casting, hot rolling and cold rolling processes were carried out to decrease the thickness of the ingot to 3 mm. Afterwards, the material was annealed 72 h at 1300 °C and 24 h at 1000 °C followed by water cooling. The average grain size of ~350 µm was obtained at this step. Equilibrating the material for 60 days at 600 °C resulted in S segregation to the GBs. Wavelength dispersive X-ray spectroscopy (WDS) measurements were conducted to detect the segregated S amount at the GBs as described in [45]. Sulfur was the only segregated element detected at the GBs. The S measurement profiles alongside the corresponding SEM images of the GBs are shown in Fig. 1. The measured S content was corrected by obtaining the GB angle relative to the sample surface using a FIB (Table 1). According to the measurements, the amount of S at the GB can vary between 27 and 57 ng cm^{-2} .

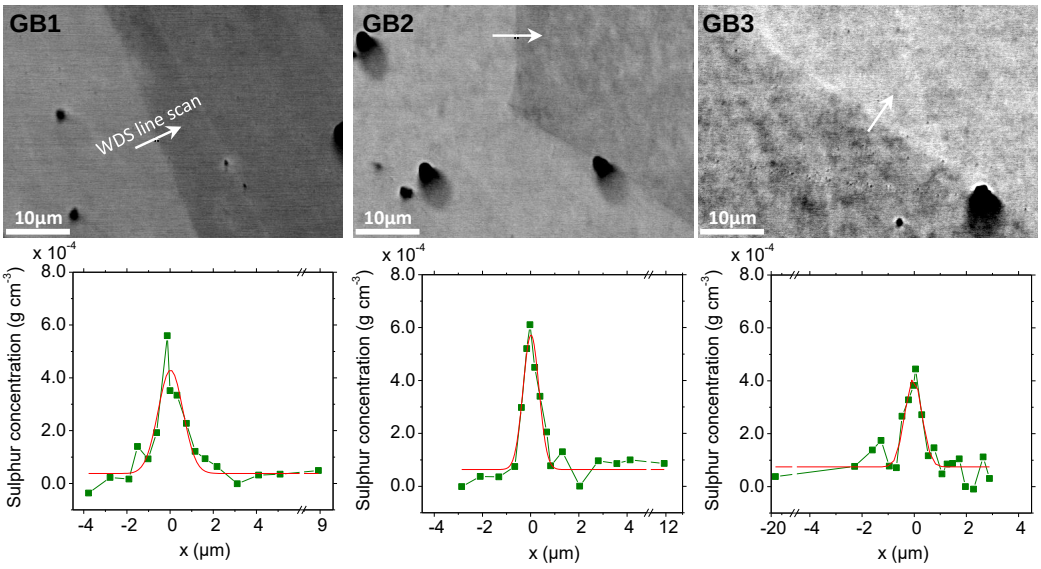

Figure 1: Sulfur concentration profiles of three different GBs across the indicated lines in the SEM images measured by WDS on the Ni sample with 5.4 wt.ppm. bulk S, annealed 60 days at 600 °C.

Table 1: Sulfur content and structural information of the selected GBs

GB ID	WDS measured GB S content (ng cm^{-2})	GB angle vs. sample surface (°)	Corrected S content (ng cm^{-2})	Sigma	Misorientation angle (°)
GB1	56.8	82.4	56.3	-	54.2
GB2	41.9	28.8	20.2	-	3.6
GB3	27.3	92	27.3	5	35.6

The sample surfaces were prepared by normal grinding and finally electropolished in a solution of 1 Molar methanolic H_2SO_4 to reach a maximum surface roughness of ~1 nm in a surface with an area of 100 μm^2 [46]. The electropolishing process was carried out at 30 V for 30 s. EBSD characterization was used to select the GBs of interest in both pure and S-doped Ni samples.

2.2. *Micro-cantilever milling and testing*

Bi-crystal micro-cantilevers were milled by the FEI Helios DualBeam™ FIB system on the GBs listed in Table 2 and highlighted by arrows in Fig. 2(a) and (b) to the dimensions presented in Fig. 2(c). The GB angle relative to the sample surface was checked to be in the range of 80–90° prior to milling of the bi-crystal beams as shown in Fig. 2(c_1) and (c_2). The tested GB in the pure Ni sample is named PNi1. For the S-doped Ni samples, one with a random GB was named NiS1 and another sample with a Σ5-type GB was named NiS2. To obtain a clean surface, the ion current density of 98 pA at 30 kV was selected during the final cleaning step. To intentionally intensify the stress concentration to the GB, a notch with the very low current density of 9.8 pA was milled aiming the GB to be positioned directly below the notch.

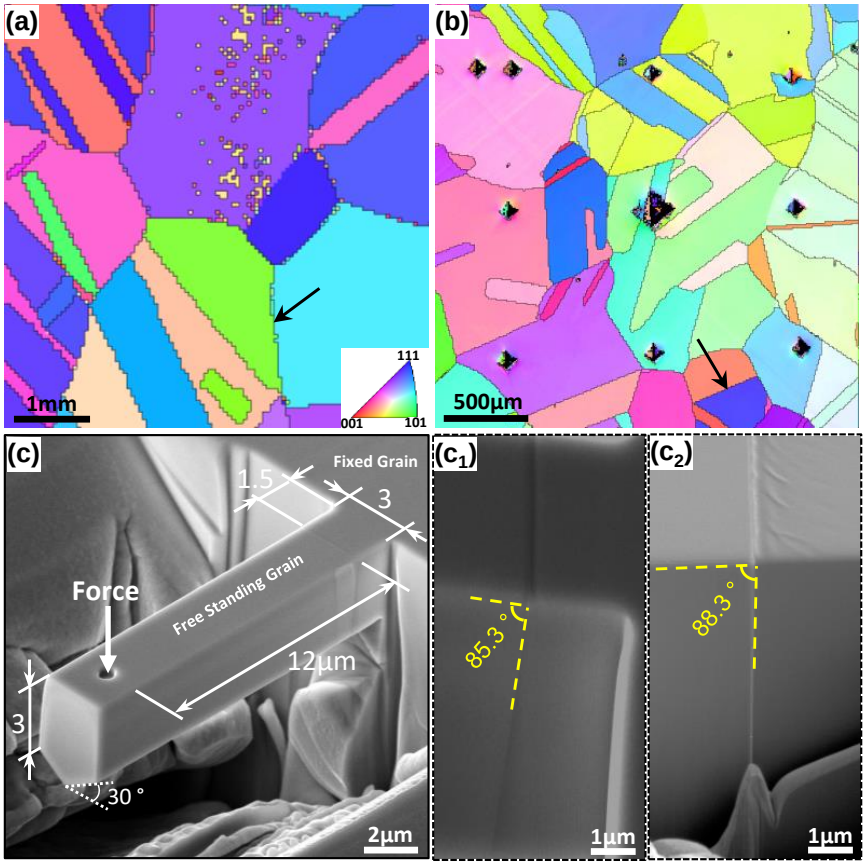

Figure 2: Inverse pole figure map of the studied (a) pure Ni and (b) S-doped Ni samples. The selected GBs for cantilever milling are marked by black arrows. (c) Representative dimensions of the bi-crystal cantilevers. Selected GB angle to the sample surface in (c_1) pure Ni and (c_2) S-doped specimen NiS1.

The micro beam bending tests were performed in two H-free and in situ electrochemical H-charged conditions using Hysitron TI 950 TriboIndenter® system. Displacement control mode was used to bend the cantilevers with a displacement rate of 2 nm s^{-1} at room temperature. A long shaft conical tip with a nominal tip radius of 500 nm was used for bending the cantilevers in liquid. A miniaturized three-electrode electrochemical setup consisting of a platinum counter, working (test material), and $Hg/HgSO_4$ reference electrodes was used in this study. The reference

electrode was connected to the cell through a double junction integrated to the TriboIndenter to perform the in situ bending tests [47, 48].

The micro-beams were charged with a cathodic current density in the range of -60 to $-100\,\mu A\,cm^{-1}$ at -1450 to $-1600\,mV$ potential versus the $Hg/HgSO_4$ reference electrode. A glycerol-based solution with the composition of 1.3 M borax in glycerol mixed with 20 % distilled water was used as the H-charging electrolyte [49]. Additional bending tests were performed on the GB called NiS2, which was H-charged by the glycerol-based solution with the addition of 0.002 M $Na_2S_2O_4$ to the solution as the H-recombination poison. High-resolution SEM imaging and cross-sectional slicing by FIB were used to track the crack propagation path versus the GB position.

Table 2: Measured GB misorientation angle and corresponding information in pure Ni (PNi1) and S-doped (NiS1 and NiS2) specimens.

GB ID	Misorientation angle (°)	Axis			Sigma	Plane 1 (fixed grain)			Plane 2 (free-standing grain)		
		h	*k*	*l*		*u*	*v*	*w*	*u*	*v*	*w*
PNi1	47.3	−2	12	19	-	16	19	14	−4	−29	−8
NiS1	46.6	21	5	16	-	−9	−4	4	2	−21	−12
NiS2	35.6	1	−29	1	5	18	−17	10	18	−17	9

2.3. Computational details

Spin polarized DFT calculations have been performed using the projector-augmented wave (PAW) [50, 51] method as implemented in the Vienna *Ab initio* simulation package (VASP) [52, 53]. The Perdew–Burke–Ernzerhof (PBE) form of generalized gradient approximation (GGA) has been used for the exchange-correlation potential [54]. The plane-wave basis set cutoff energy has been set to 400 eV. The convergence criteria of self-consistent calculations have been set to 10^{-5} eV/cell for the total energy and to 9×10^{-3} eV/Å for the atomic forces. The integration over the Brillouin zone has been done using the $4 \times 4 \times 1$ Monkhorst–Pack *k*-mesh [55] for all slab geometry calculations and using the $4 \times 4 \times 4$ *k*-mesh in the $3 \times 3 \times 3$ (conventional FCC cell) bulk supercell calculations. The lattice parameter has been fixed to 3.515 Å [29] and only the ions have been allowed to relax in all slab and bulk calculations. The Ni $\Sigma5(012)$ coincidence site lattice (CSL) symmetric tilt GBs has been modeled using a 76-atom GB slab with 19 layers and 4 atoms/layer [29]. The Ni $\Sigma5(012)$ GB structure used in this work and an illustration of GB cleavage are shown in Fig. 3.

The site preference of H and S impurities in the bulk of FCC Ni has been studied by means of DFT calculations in a number of publications [28, 29, 56–58]. The results have shown that H prefers to occupy the octahedral interstitial site [28, 29, 57, 58] and S substitutes the lattice sites [56, 57] in the bulk. Here, we use these results and define the GB segregation energy as the total energy difference between the bulk of the material with an impurity atom occupying the most-stable site (interstitial octahedral for H and substitutional for S) and the system with an impurity atom situated at the GB (both substitutional and interstitial sites are considered). The methodology to obtain GB segregation energies (E_{seg}^{gb}) and the work of separation W_{sep} from DFT calculations is described in detail in [10, 29].

The GB enrichment of H and S at $T > 0$ has been modeled by means of a modified McLean isotherm [1, 41–43], which takes as input GB segregation energy profiles from DFT calculations. In contrast to the classical equilibrium segregation isotherm, the used model considers the possible effects of grain size (solute depletion in the bulk) and the kinetics of segregation. The details of the model are given in [42, 43].

The ideal work of separation W_{sep} is a fundamental thermodynamic quantity that controls the mechanical strength of an interface. It has been chosen to evaluate the resistance of the selected GB to decohesion. A reduction in W_{sep} indicates a reduction in the cohesive strength of an interface. However, it does not automatically mean that the interface will fracture in a brittle manner [3]. Another condition has to be satisfied: $W_{sep} < G_{disl}$, where G_{disl} is the minimal energy per unit area of crack advance required to emit a single dislocation. This energy can be estimated to be in the range between 1 and 3 J/m^2 for Ni depending on the applied shear stress level, orientation of the GB, temperature, and the stress rate [59]. An alternative way of estimating the brittle to ductile fracture mode is *R*, i.e., the ratio of W_{sep} to twice the free surface energy of the metal [60, 61]:

$$R = \frac{W_{sep}}{2\gamma_{fs}^{PCP}}, \tag{1}$$

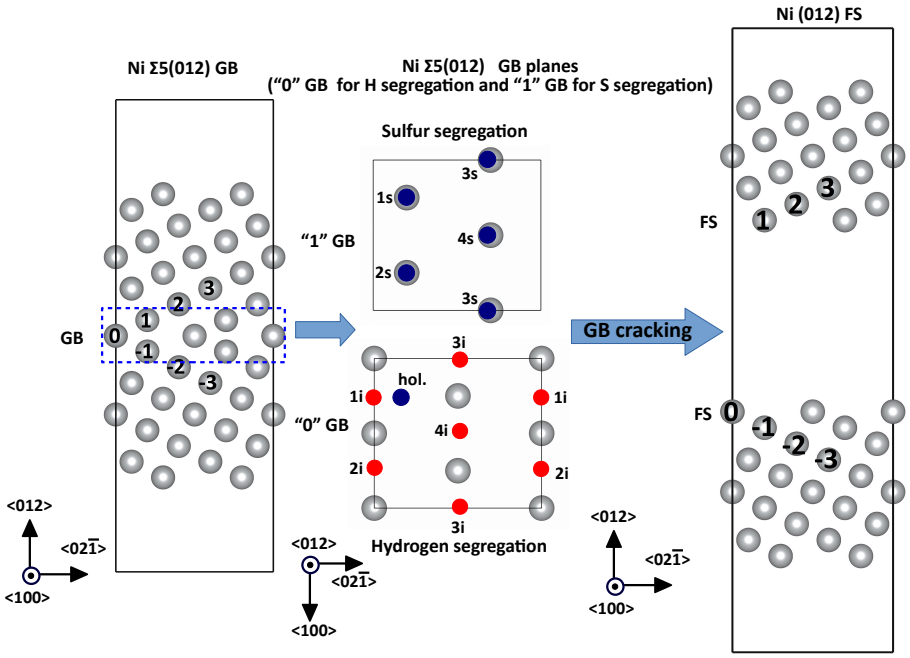

Figure 3: Illustration of cracking at Ni Σ 5 (012) [100] symmetric tilt GB. GB layers "0" and "1" with interstitial H and substitutional S atoms are also shown.

where γ_{fs}^{PCP} denotes the surface energy of the preferred cleavage plane, which for FCC metals is mainly the (111) plane [62]. Free surface energy of Ni (111) surface is obtained by $\gamma_{fs}^{PCP} = (E_{fs}\text{-}N * \epsilon_0)/2A_{fs}$, where E_{fs} is the total energy of the surface slab, N is the total number of atoms, and A_{fs} the area of surface slab. If R is close to unity, transgranular cleavage is expected, whereas for lower values IG fracture is expected.

3. Results

3.1. Bending of the bi-crystal micro-cantilevers

3.1.1. Pure nickel GB

Fig. 4(a) shows the representative load–displacement (*L–D*) curves of the pure Ni bi-crystal micro-beams obtained in two different experimental conditions of H-free environment and in situ electrochemical H-charging for 2 and 3 h. Although the elastic stiffness is well matched for the two sets of the curves and all the tested beams have a relatively similar yield point, there are obvious differences in the plastic regime. The cantilever bent in H-free condition shows slight hardening up to reaching the maximum load at ~2.5 μm displacement follows by gradual reduction in the flow curve to the final 5 μm displacement. From Fig. 4(a) it can also be inferred that the work hardening rate of the H-charged beams is higher than in the H-free condition. In addition, the maximum load of the H-charged beams reaches higher values in comparison with H-free beams. The same phenomenon is reported for Ni–H systems by others and it is believed that the interaction between H and dislocations can be the reason for such increases in load and hardening rate [63]. In the case of H-charged beams, the reduction in the flow curve place at a displacement of ~1 to 1.5 μm. The continuous decrease in the loading force of the H-charged beams can be an indication for the H-induced cracking and decrease in the cross-sectional length of the beams, which leads to a reduction in the required force for the test continuation.

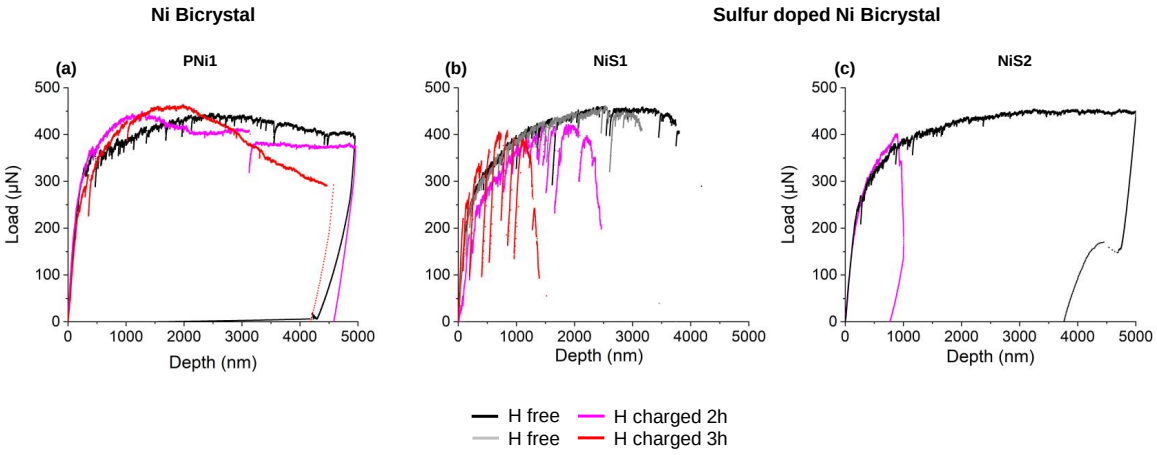

Figure 4: Load–displacement curves of the (a) pure Ni (GB PNi1 in Table 2) and (b) and (c) S-doped (GBs NiS1 and NiS2 in Table 2, respectively) bi-crystal beams tested with H-free and in situ electrochemical H-charging conditions.

Fig. 5(a_1)–(a_3) and (b_1)–(b_3) shows the post-deformation micrographs of the pure Ni bi-crystal beams bent in H-free and H-charged conditions, respectively. As is evident from Fig. 5(a_1 and a_2) for the H-free condition, the notch is blunted along abundant slip traces visible in the top and the cross-sectional surfaces in adjacent crystals of the beam. According to Schmid's law, the observed slip traces in the free-standing and the fixed side of the bi-crystal beam are due to the activation of the dislocation on the $(-1\ -1\ 1)$ plane in fixed-grain and the $(1\ -1\ -1)$ plane with Schmid value of 0.35 and 0.48, respectively. This phenomenon demonstrates that the plasticity during the deformation is not only present in the notch area, but also spreads out to the fixed and free-standing grains in the bi-crystal beam as shown by yellow dashed lines. Fig. 5(a_3) and (a_4) exhibits the GB positioned beneath the notch withstanding the plasticity with no evidence of IG cracking. The schematic diagram shows the deviation of the GB from its original straight form, which displays a great amount of plasticity beneath the notch. The observed chain of the micro-voids in the notched

area (Fig. 5(a_3)) is also a strong proof for the domination of plasticity in the H-free beams. In contrast to the beams bent in the H-free condition, crack propagation from the notch position was observed for the H-charged beams, which was the reason for the continuous decrease in the corresponding *L–D* curve in Fig. 4(a). A closer cross-sectional view of the cracked beam in Fig. 5(b_2) illustrates fewer slip traces compared with H-free tested beams, which is an indication for the lower plasticity and its confinement to the notch area in the H-charged beams. From this figure, it is also obvious that the crack did not follow the GB path as depicted in the schematic diagram. Alternatively, it has initiated from the notch itself and propagates in zigzag-shaped form in the fracture surface. Further slicing through the thickness of the beam by the FIB (Fig. 5(b_4)) has also demonstrated that the crack is not IG and it propagates to the neighboring grain.

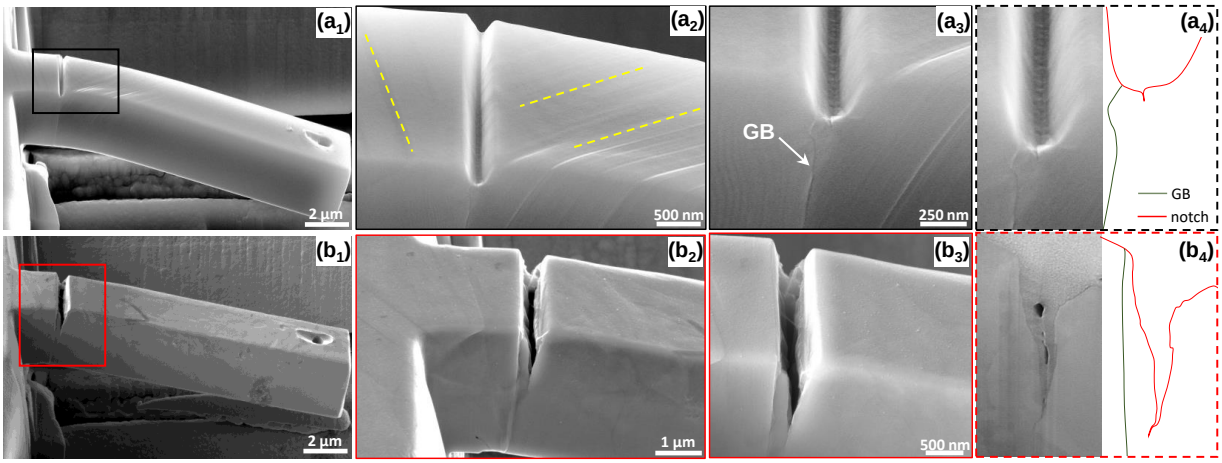

Figure 5: Post-deformation secondary electron images from the side view of the pure Ni bi-crystal beams (GB PNi1 in Table 2) tested with H=free (a_1)–(a_3) and in situ H-charging (b_1)–(b_3) conditions.

3.1.2. Sulfur-doped GB

The *L–D* curves of the S-doped bi-crystal beams with the GB NiS1 and NiS2 are shown in Fig. 4(b) and (c), respectively. For NiS1 cantilevers, the bent beams show a rapid decrease in the load after reaching a maximum load of ~450 and ~400 µN in the H-free and H-charged environmental conditions, respectively. The sharp load reduction with considerably higher slope compared with the pure Ni results is attributed to the detrimental effect of the S impurity segregation to the GB. Testing the beams in the H-charged condition decreased the displacement to about 2.5 and 1.5 µm after 2 and 3 h of charging. However, the GB embrittling degree of the material is strongly dependent on the content of the segregated elements and also the type of the subjected GB. To investigate this, another type of GB with different misorientation angle and segregated S content was examined. Fig. 4(c) shows the *L–D* curve of the NiS2 GB with 27.3 ng cm^{-2} S. This GB is a Σ5 type and has around 11° misorientation lower than the NiS1. In the H-free condition, no rapid load drop is observed in NiS2 in contrast to NiS1 beams and the load is leveled off on the maximum load of ~450 µN up to the final displacement of 5 µm. However, introducing H into the S-doped GB caused a distinct change in the *L–D* behavior compared with the H-free condition. A reduction in the final tolerated displacement to 1 µm is a strong indication of the combined effect of H and S atoms in weakening the GB.

Post-deformation micrographs of the beams containing the GBs of NiS1 and NiS2 bent in H-free testing condition are shown in Fig. 6(a_1)–(a_4) and (b_1)–(b_4), respectively.

The NiS1 bi-crystal beam shows a straight and sharp GB opening with a complete brittle-type fracture surface, which cut the notch area and results in the formation of a jagged-shaped cleavage pattern in the coincidence place of the GB and the notch. This is depicted in the Fig. 6(a_3) and (a_4). From the figure it can also be inferred that the stress concentration in NiS1 is mostly localized at the GB and fewer slip traces can be observed in the neighboring grains. By contrast, the greater plasticity of NiS2 compared with NiS1 can be elucidated from the abundant and spread slip traces especially in the free-standing side of the beam. Although a crack nucleation can be observed in the GB (as noted in Fig. 6(b_3) and (b_4), the notch blunting and high plasticity prevail in the deformation process. Thus, it can

be deduced that in both S-doped GBs (NiS1 and NiS2), the crack is initiated from GBs rather than the notch area. However, owing to dissimilarity of the GBs, the severity of the GB opening was different. In NiS1, the GB opening reaches the notch area, whereas in NiS2, it was stopped before reaching the notch surface. The different behavior of these two GBs are more significant considering that the final displacement of the beam containing GB NiS2 was 5 µm whereas for the NiS1 sample the displacement was about 3 µm at the stage of the sharp load drop as shown in Fig. 4(b) and (c).

For both types of GBs, the co-existence of H alongside S caused the complete brittle fracture in the GB plane as shown in Fig. 7. The angled crack path in the remaining fixed side of the beams shown in Fig. 7(a_2) is an indication that the crack follows the GB. Accordingly, the sharp crack propagation in the NiS2 GB after 2 h H-charging was represented by a sudden load drop at ∼1 µm displacement in the *L–D* curve as shown in Fig. 4(c). It should be noted that the used solution for H-charging of the beams with NiS2 GB contained the H recombination poison. The presence of recombination poison lead to diffusion of more H into the metal and therefore the crack nucleation and propagation happened at a very low displacement in comparison with beams tested in the poison-free solution (Fig. 4(b) and (c)).

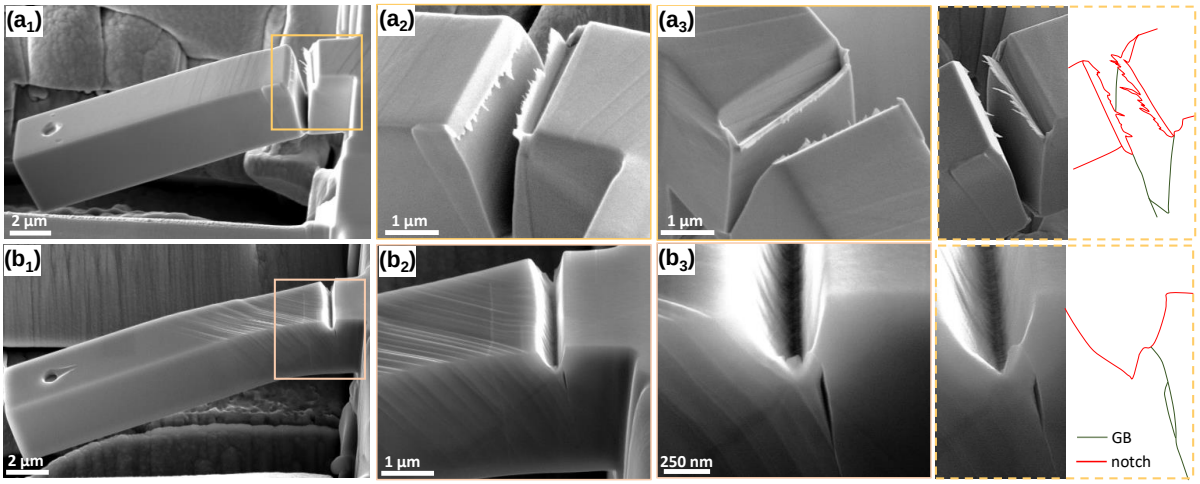

Figure 6: Secondary electron images from the side view of the bi-crystal beams on the S-doped sample for (a_1)–(a_3) NiS1 and (b_1)–(b_3) NiS2 in Table 2 bent with H-free condition.

3.2. Computational results

3.2.1. H and S segregation to Ni GBs

The calculated GB segregation profiles of 0.25 ML of H and S impurities located in the first four GB layers as a function of distance from the GB plane are shown in Fig. 8. The results are found to be in good agreement with data available in the literature [28, 29, 64]. In Fig. 8, one can see that H prefers to occupy the interstitial sites within the GB layer (GB layer "0" in Fig. 3). Specifically, H prefers the "bridge" interstitial sites (shown by 1i–4i in Fig. 3). S, on the other hand, has the lowest segregation energy corresponding to its segregation to the substitutional sites (1s–4s) in the positions next to GB ("1") layer. Our results also show that there is a small energy difference between the substitutional site and the "hollow" interstitial site for S (shown in Fig. 3 by *hol.* in the "0" GB layer). The calculated segregation energy of −1.59 eV/atom for S is in good agreement with previous DFT investigations [64] and experimentally measured value of −1.48 eV/atom [65]. We have also found an additional not reported earlier segregation site for S atoms located at the interstitial inter-space between layers 0 and 1 with the energy of −0.75 eV/atom.

In addition to segregation profiles, we have investigated the effect of the GB excess on the segregation energy of H and S. In Fig. 9, we show the E^{gb}_{seg} dependence on the GB excess of segregating elements ranging from 0.25 to 1 ML impurity excess for their preferred segregation site (only the minimum energy configuration for each GB excess is shown). H exhibits virtually no GB excess dependence with only a very shallow local minimum of the segregation energy at 0.5 ML GB excess, which has been observed in a number of previous DFT investigations [29, 66, 67]. In

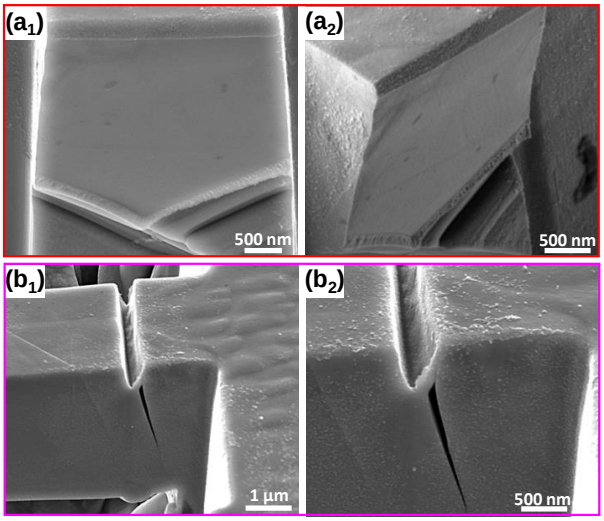

Figure 7: Secondary electron images from the fracture surface of the beam for NiS1 (a_1) and (a_2) and the crack propagation path in NiS2 (b_1) and (b_2) bent with in situ electrochemical H-charging condition.

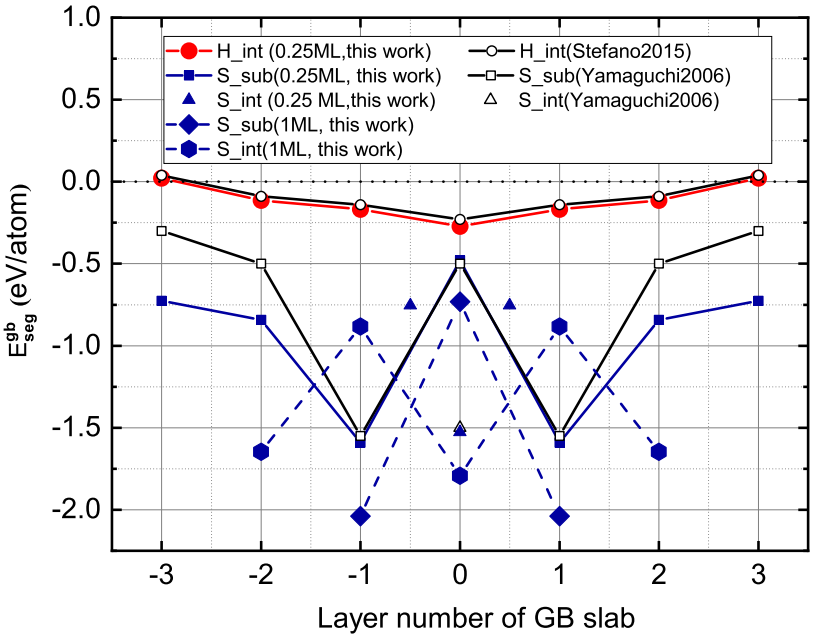

Figure 8: H and S segregation profiles at Σ5 (012) GB in Ni compared with data from the literature [28, 64]. The S segregation energies are shown for 0.25 and 1 ML coverage by using solid and dashed lines, respectively. The layer numbers corresponding to the segregation energy profiles are shown in Fig. 3.

contrast, S atoms show an attractive interaction with approximately 0.20 eV/atom reduction in E_{seg}^{gb} when S GB excess is increased from 0.25 to 1 ML. This result is in good agreement with the theoretical results of [10, 64] and the results of an experimental investigation in [68], where the observed S content at the GB was estimated to be in the range of about 1 ML. Similar interactions are present for S at other sites, as can be seen in Fig. 8 for increasing the coverage from 0.25 ML (solid lines) to 1 ML (dashed lines).

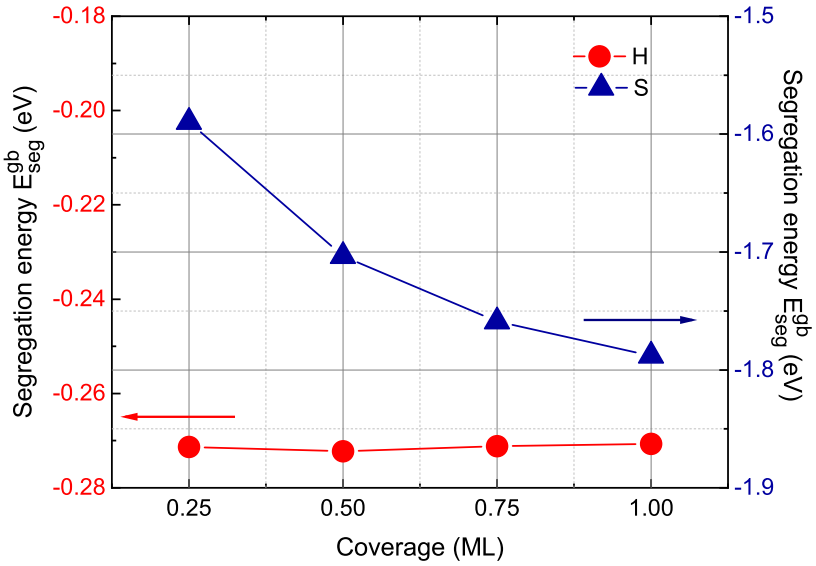

Figure 9: Coverage effect on H and S GB segregation energies. Segregation energy per atom for coverages from 0.25 to 1 ML for interstitial H at site "0" is shown on the left y-axis, whereas the same for substitutional S at site "1" is shown on the right y-axis.

3.2.2. Interaction between segregating atoms at GB

The interaction energies between H and S atoms at the GB in Ni have been investigated by DFT calculations and the results are listed in Table 3. The interactions have been obtained for four different S and H GB excesses (0.25, 0.5, 0.75, and 1 ML) and only the minimum energy configuration for each GB excess are listed in the table. The interaction energy between the impurity atoms located at the GB E^{int} has been defined as

$$E^{\text{int}} = E^{\text{gb}}_{\text{slab}}[N-n;m;n] + (n+m-1)E^{\text{gb}}_{\text{slab}}[N;0;0] - mE^{\text{gb}}_{\text{slab}}[N;1;0] - nE^{\text{gb}}_{\text{slab}}[N-1;0,1], \quad (2)$$

where $E^{\text{gb}}_{\text{slab}}[N;m;n]$ is the total energy of the GB slab with m H atom(s) and n S atom(s) at the GB, $E^{\text{gb}}_{\text{slab}}[N;0;0]$ is the energy of a slab with no impurity atoms, $E^{\text{gb}}_{\text{slab}}[N;0;n]$ is the energy of a slab with n S atoms, and $E^{\text{gb}}_{\text{slab}}[N;m;0]$ is the energy of a slab with m H atoms. Negative values of E^{int} correspond to attractive interaction of the atoms at the GB.

The results for the interaction energy of H with itself and S with itself show the same as Fig. 9 with negligible interaction for H and significant attractive interaction for S. If we look at the interaction of H in the presence of 0.25 ML S, the interactions become repulsive. In addition, in the case of S in the presence of 0.25 ML H, the interactions are less attractive than in the case of only S interacting with itself. The results show that there are weak repulsive interactions between H and S atoms. The absolute value and the repulsive character of H–S interactions suggest that the GB segregation of S atoms should not be strongly affected by H co-segregation and vice versa. The main factor influencing S GB enrichment is the concentration of S at the GB, whereas the GB segregation of H seems to be quite inert to any GB compositional changes.

3.2.3. Kinetics of H and S segregation to Ni GB

The enrichment of the GB with S and H atoms has been calculated using the DFT segregation profiles shown in Fig. 8 (corresponding to 0.25 ML GB excess for H and 1 ML for S) and the segregation models described in[42, 43]. Following the results of the previous sections, the interactions between H and S atoms have been neglected. The results on S enrichment have been obtained by concentration averaging over the interstitial and substitutional positions in the first three GB layers, whereas only interstitial positions have been considered in the case of H enrichment. The average grain size of 350 μm and the initial bulk amount of S equal to 5.4 wt.ppm. (10 at.ppm.) have been taken from the

Table 3: Calculated interaction energies between the segregating elements at the GB E^{int}(eV), work of separation (J/m^2), the reduction in the work of separation (%), and the ratio R calculated from Eq. (1).

GB system	GB coverage (ML)		E^{int}	W_{sep}	$\Delta W_{\text{sep}}(\%)$	R
	S	H				
Ni	–	–	–	3.508	–	0.91
Ni+H	–	0.25	–	3.414	−2.69	0.89
	–	0.50	−0.002	3.321	−5.33	0.87
	–	0.75	0.000	3.201	−8.75	0.83
	–	1.00	0.002	3.084	−12.09	0.80
Ni+S	0.25	–	–	3.187	−9.19	0.83
	0.50	–	−0.228	2.927	−16.62	0.76
	0.75	–	−0.508	2.628	−25.13	0.69
	1.00	–	−0.793	2.286	−34.88	0.60
Ni+(S & H)	0.25	0.25	0.061	3.106	−11.47	0.81
	0.50	0.25	−0.102	2.797	−20.28	0.73
	0.75	0.25	−0.296	2.524	−28.06	0.66
	1.00	0.25	−0.567	2.178	−37.93	0.57
	0.25	0.50	0.120	2.967	−15.42	0.77
	0.25	0.75	0.154	2.839	−19.08	0.74
	0.25	1.00	0.223	2.701	−22.99	0.70

results of Section 2.1. The information about H content in the Ni samples during charging has been estimated to vary from 50 to 300 at.ppm. The GB width has been taken from the segregation energy profiles shown in Fig. 8 equal to 8 Å. The bulk diffusion has been taken into account via $D = D_0 \exp E_a/k_B T$ with $D_0 = 1.4 \times 10^{-4}$ m/s^2; $E_a = 2.28$ eV [69] and $D_0 = 4.47 \times 10^{-7}$ m/s^2; $E_a = 0.37$ eV [70] for S and H in Ni, respectively. The grains have been discretized into shells with a thickness of 1 μm. The information about the heat treatment history of the sample has been taken from Section 2.1 and is divided into two intervals of interest: (I) annealing; (II) H-charging.

The modeling results are shown in Fig. 10, where the left-hand side of the figure refers to the three-step annealing process (stage I) of 1300°C for 72 h → air cooling (t' = 10°C/s) → 1000°C for 24 h → water cooling (t' = 100°C/s) → 600°C for 60 days and the right-hand side to H-charging at 300°C for 10 h. The top panels show the evolution of temperature as a function of time. The bottom panels show the amount of S and H segregating to the GB in Ni as a function of the heat treatment time.

During the simulated three-step annealing process, S enrichment at the GB reaches 75 at.% at the end of stage I. This value is slightly below the theoretical equilibrium enrichment of S at 600°C of 78 at.% and suggests that S has almost reached its equilibrium concentration at the GB. Note that the equilibrium S GB excess at the room temperature is about 100 at.% and the obtained amount of 75 at.% of S at the GB is a result of the instant quenching from 600°C to room temperature at the end of stage I. The content of S remains constant during the H-charging (stage II) as diffusion is too slow at this temperature to lead to enrichment. In contrast, the amount of H diffusing into the GB after charging (stage II) varies from 10 to 18 at.%, which corresponds to the equilibrium values for the assumed H content from 50 to 300 at.ppm. in the bulk of Ni, respectively. In summary, we estimate about 75 at.% of S and 10–20 at.% of H at the GB after stages I and II of the heat treatment at the selected Σ5(210) GB.

The calculated S GB content of 75% (after stage I heat treatment in Fig. 10) can be compared with the estimated S GB concentration from the experimental WDS measurements of S segregation profiles listed in Table 1. To do so, we have converted S GB content values reported in ng/cm^2 into ML using a conversion factor reported in [68]. The theoretical prediction of S GB excess after stage I heat treatment should be close to the experimental GB S content at the GB with the highest misorientation angle, i.e., GB1 from Table 1. Indeed, our calculated value of 75% corresponding to 0.75 ML/layer on average for the given GB is in reasonably good agreement with the experimental value of 0.84 ML from the WDS experimental measurements. Here, it should be noted that GB excess of impurity atoms is highly dependent on the GB structure and the current comparison is valid under the assumption that both theoretical and experimental GB structures are close to each other.

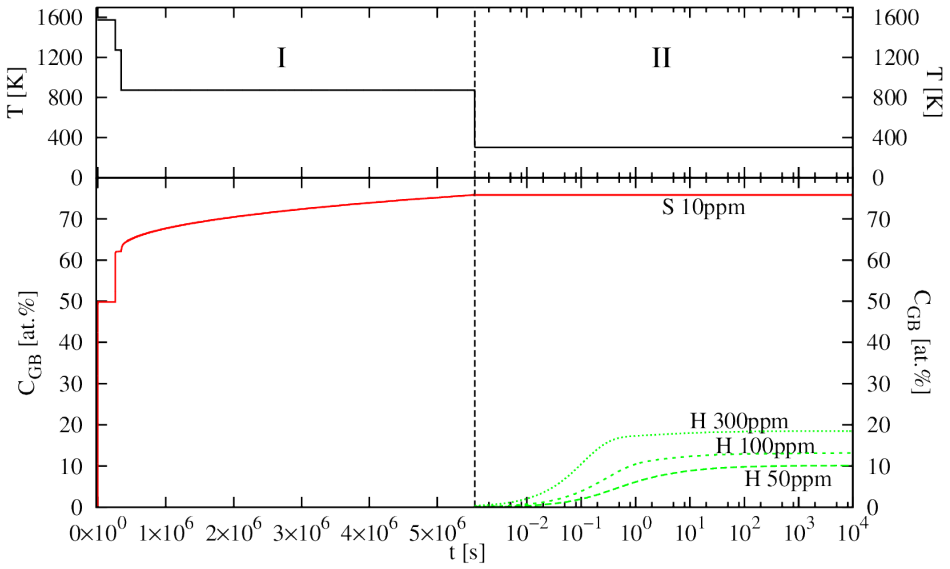

Figure 10: Enrichment of S and H at Ni GB as a function of temperature and time. The upper panel shows temperature evolution during sample preparation and H-charging. The dashed vertical line splits the two stages of sample treatment: (I) three-step annealing and (II) H-charging. Assumed bulk concentrations of S and H in the calculations are given next to the corresponding concentration profiles. All concentrations are given in at.% and at.ppm.

3.2.4. GB decohesion by H and S

The effect of H and S on the W_{sep} of the Σ5(210) GB in Ni is shown in Fig. 11. Here, we show W_{sep} as a function of GB coverage x by xH, xS, 0.25S+xH, and 0.25H+xS segregating atoms. Both elements decrease W_{sep} and reduce GB resistance to decohesion. In absolute values, the effect of S on the GB decohesion is much more pronounced than that of H. In addition, variations of S GB excess (coverage) have a more pronounced effect on W_{sep} than H. However, it is the simultaneous segregation of both H and S atoms to the GB, which results in the most-pronounced GB decohesion among all considered cases. The reduction is as much as 38% (see Table 3).

As has already been mentioned in Section 2.3, reduction in W_{sep} by itself is not sufficient to describe GB embrittlement of a material. The upper estimate of G_{disl} of about 3 J/m^2 and the results presented in Fig. 11 suggest that a brittle fracture can be expected at 0.5 ML GB coverage of S atoms, whereas a significantly higher fraction of H atoms at the GB can be required to promote brittle fracture in Ni. An alternative estimate based on the calculations of the R ratio by using (1) as listed in Table 3, also demonstrates that the increase in S GB excess decreases R (reduces ductility of the GB) in a much more pronounced manner than increasing H GB excess. However, the combined effect of both H and S atoms segregating to the GB in Ni results in the most detrimental effect of all with the largest reduction in R at 1 ML of S and 0.25 ML of H GB excess. This suggests that S-rich GBs should be especially prone to HE even at low H GB concentrations. The calculated amounts of S (0.75 ML) and H (0.1–0.2 ML) at the GB after stages I and II of the heat treatment described in the previous section result in R = 0.66, which is the second lowest R value (the lowest belongs to 1 ML of S and 0.25 ML of H) with approximately 28% reduction in the work of separation (compared with pure Ni) indicating a very strong propensity towards brittle fracture of the GB.

4. Discussion

4.1. GB effect on the micro-mechanical behavior of the pure Ni bi-crystal

The presence of a GB in the microcantilever further complicates the experiment. Different grain orientations lead to activation of different slip systems to different mechanical behavior of the beam. As shown in the schematic diagram of Fig. 5(a$_4$), the high number of slip traces observed in the free-standing grain forced the GB to deviate from its original straight form to curved or so-called bulged shape [44] in the upper part of the beam beneath the notch. It seems that the GB acts as a sink of dislocations and all the activated slip systems end up on their pass at the GB

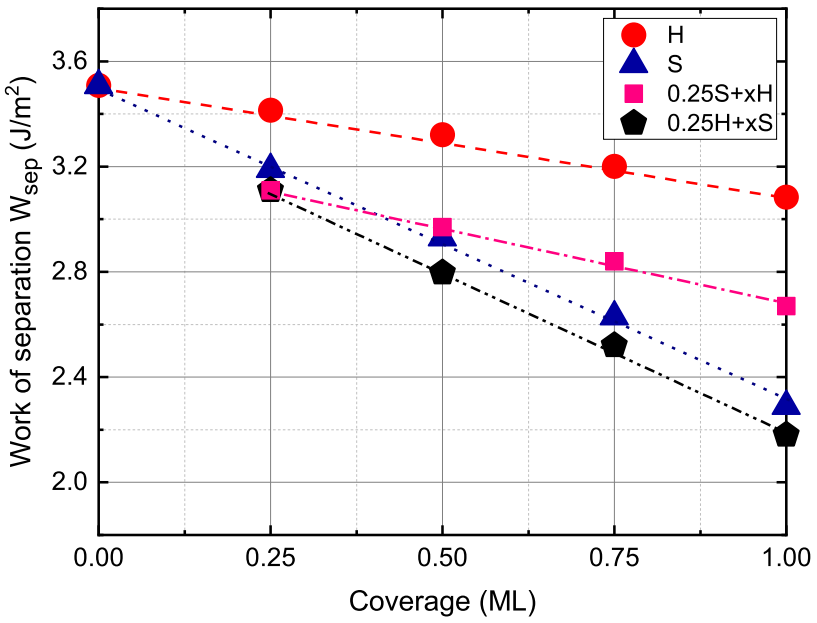

Figure 11: Coverage change effect on the GB work of separation. The work of separation values for the coverage range of 0.25–1 ML H and S individually as well as the H–S co-segregated GB are presented.

[71]. On the other hand, the chain of micro-voids formed at the root of the blunted notch represents the commence of typical ductile fracture from the notch root. Accordingly, it appears that in the tested pure Ni bi-crystal system both the GB and notch are stress-tolerated areas with a full plastic response.

Introducing H into the system causes a distinct change in the mechanical response of the tested beams. Two clear differences between H-free and H-charged tested beams can be observed.

- First, the image contrast reveals fewer surface slip traces for the H-charged sample. Similar phenomenon has been observed by Rogne et al. on Fe26Al0.5Cr intermetallic cantilevers. Where for H-charged beam the plasticity was confined to the crack area, while the slip traces spread widely far from the crack for the H-free tested beams [72]. Likewise, hydrogen assisted fatigue crack growth on a pure Fe showed that the H has a main contribution to reduce the crack tip plasticity expansion [73]. Here it can be inferred that H confines the plasticity to the stress concentrated area at the crack tip [48, 74, 75]. In the H-free case, dislocations that are formed during the plastic deformation can move easily and reach the free surface of the cantilever, resulting in slip traces. In contrast, accumulation of the H atoms at the crack tip can pin the dislocations originated from the crack tip and, hence, the plastic affected zone will be confined to a small area around the crack tip. The observed phenomenon cannot be fully interpreted by the HELP mechanism. According to this mechanism, the H ingress to the system would facilitate the dislocation emission, which result in more plasticity spread and more slip traces would reveal on the surface. In fact, plasticity localization behind the HELP mechanism in the presence of pre-notch or pre-crack confines to the crack tip. It is well agreed the high hydrogen concentration at the crack tip results in dislocation nucleation energy reduction. Therefor dislocation nucleation rate at the crack tip increases. High density of dislocations alongside with the high concentration of the H, impedes the dislocation shielding leads to their pinning at the crack tip.

- Second, in contrast to the H-free condition, the crack is initiated when the solute H was present in the material. However, the formed crack does not show fully brittle characteristics and does not follow a straight line in the same way as a brittle crack. The presence of pyramids with triangular base in the fracture surface of the created crack from the top view (Fig. 5(b_3)) is evidence that the crack propagation is accompanied by the plastic deformation. In addition, the *L–D* curves (Fig. 4(a)) also show not a sudden but gradual load drop during the

deformation, which is also an indication of the accompaniment of the plastic deformation beside the crack propagation. The plastic growth of the crack in the H environment, which is actually a mixture of plastic blunting and cracking, has been reported a long time ago [76]. The concentration of H at the very tip of the crack lets the crack grow in a stable manner to a certain extent by micro-cleavage and then the crack growth continues by plastic deformation with the concomitant of dislocations from the crack tip up to reaching a critical H concentration for the next micro-cleavage growth [14]. The rough fracture surface in the H-charged sample can be an evidence that the H amount in the fracture process zone was not enough to induce smooth fracture surfaces. Researching on the Ni single crystal, Vehoff reports that at constant temperature, the fracture surface roughness of the sample increases as the H pressure in the testing chamber decreases [14].

Interestingly, the GB present in the bi-crystal system did not act as a crack nucleation area during the H-charging test and crack propagation stage. It seems that in this case, the GB does not act as a strong H trap. In general, unlike many body-centered cubic (BCC) metals, FCC metals have a relatively high solubility of H. In addition, knowing that the diffusivity of H is significantly lower than in BCC metals, one would expect that H enrichment is rather low in FCC metals. The study of Pu and Ooi [77] on austenitic stainless steel using a silver micro-print technique reported that the GB in FCC alloys is not an important trap for H. In the review study of McMahon on steels [78], it is suggested that H cannot induce IG cracking, unless other embrittling elements are presented in the alloy. However, some conflicting results have been published. Lassila and Birnbaum [79] reported a brittle fracture in the presence of H, but they also mentioned that as long as the H concentration is not more than the H contained in solid solution, no brittle fracture was observed. The reason behind this discrepancy in the literature can be related to the fact that the specific GB misorientation can be another factor that must be considered. It is reported that different GB misorientations tend to result in different amounts of H enrichment as well as diffusivity [80, 81]. Oudriss et al. [80] suggested that the diffusible H along random GBs may be the major cause of HE. However, in our case of the random GB, the effect of H was not enough to induce complete brittle fracture. The same results were obtained by Tehranchi and Curtin [19, 82]. Investigating pure Ni GB, they concluded that Ni GBs show no noticeable propensity for H to induce significant embrittlement and the presence of H creates no ductile-to-brittle transition. Another parameter that should be considered for the analysis of the results is the amount of H that is charged into the sample. The brittle type of fracture is often correlated in the literature with the amount of H dissolved in the material. Vehoff and Rothe [14] stated that the room temperature equilibrium concentration of H in the fracture process is the controlling factor for HE. The H concentration is controlled by the stress field of the plastic zone and by the type and number of traps presented in this zone. According to their results, the IG cracking may be initiated and replaced by transgranular cracking if the H activity is further enhanced by cathodic charging during the test. This point is discussed in more detail in the following sections.

4.2. GB S segregation effect on the micro-mechanical behavior of the Ni bi-crystal

S is known as a harmful impurity that if enriched at the GB, would have a detrimental effect on the mechanical properties of the GB and, consequently, the entire material. In comparison with the pure Ni beam, which shows a ductile behavior and notch blunting, the observed IG crack initiation and propagation in NiS1 and NiS2 GBs (Fig. 6) is a clear indication of the detrimental effect of the segregated S.

Several reasons have been proposed to show how the S enrichment changes the ductile behavior of a GB to a brittle IG fracture. Changes in the electronic structure that weaken the Ni–Ni bonds in the GB have been reported by Messmer et al. [83]. Yamaguchi et al. [84] suggested the large GB expansion owing to the dense S segregation can decrease the cohesive strength of the Ni GB up to one order of magnitude. It is stated that the S–S bonding formed in the GB, which is calculated to have about 24% larger distance compared with the Ni–Ni or Ni–S pairs leads to expansion in the surrounding Ni–Ni and Ni–S bonding. Consequently, this expansion in Ni–Ni or Ni–S bonds are responsible for weakening and decohesion of the GB.

The DFT results provided in Fig. 11 and Table 3 indicate that S segregation has a major effect on the decrease in W_{sep}. This increases the propensity for IG fracture if one considers the R ratio calculated in Table 3. Here, we have attempted to correlate the value of R with experimental observations of the fractured surfaces with and without H and S and concluded that the brittle fracture may occur in the materials under investigation at $R < 0.8$ (see Section 2.3 for details). Thus, the segregation of 0.5 ML of S or greater can lead to the brittle fracture.

Although both NiS1 and NiS2 show a brittle crack at the GB, the strength of the GBs against crack propagation and therefore their response to the mechanical loading presented in *L–D* curves were different. Three factors are proposed to explain this difference.

(a) Geometry effect. The location of the GB beneath the notch and also the angle of the GB to the cantilever surface can affect the stress intensity and, hence, mechanical behavior of the system. From an experimental point of view, it is important to have a perpendicular GB plane to the specimen surface and also to the load axis. In this way, it can be assured that the activation of the slip bands, which are oriented nearly parallel to the GB plane, will be suppressed. Moreover, the tensile stress concentration will be the maximum within the GB plane assuming that the pure tensile stress dominates on the beam surface at the beginning of the test. Furthermore, the actual GB position relative to the notch should be taken into account. In order to keep the consistency of stress distribution around the GB, the notch should be milled similar in all testing beams. Small deviations in the notch position relative to the GB plane can lead to redistribution of the stresses in the plastic deformation zone. In this work (see Section 2.1, we attempted to reduce the effect of the aforementioned geometrical factors to a minimum. Comparing the notch and GB system in Fig. 6 it can be inferred that for both NiS1 and NiS2, the GB is positioned at a distance of several tens of nanometers aside from the notch root. Therefore, we assume that the geometry has a minor effect on the presented results in comparison with other parameters.

(b) Structural effect. The type as well as the misorientation of the GB has been reported to have an influence on the crack initiation and propagation. High-energy random GBs are supposed to have weak resistance to the fracture whereas low-energy and low-angle GBs are more resistant [85]. In a work on Mo bi-crystals, values of fracture stress were observed to vary by a factor of six by changing the misorientation angle [86]. Thus, the different misorientation angle of the NiS1 GB compared with NiS2 can play a key role to show a nearly complete rupture of the GB to the surface. The incompatibility factor of the GB can also play a role in the observed difference. Vehoff et al. [14] showed in their experimental work on S-doped GBs that the IG cracking susceptibility increases by adding an elastic–plastic incompatibility to the bi-crystal system. Having the constant amount of S in the GBs, they investigated the effect of incompatibility by switching from a symmetrical tilt GB to an asymmetrical GB between hard and soft grains. The results confirmed that the high stress concentration associated with the incompatibility can be one of the controlling factors of the IG fracture. In our work, the NiS2 GB has a symmetric nature as an Σ5-type GB, whereas NiS1 is an asymmetric GB. Thus, again, this factor can be another parameter to enhance embrittling potency of the NiS1 GB.

(c) Chemical effect. This factor is closely related to the structural effect, as a different nature of the GB leads to a different amount of S that can segregate. In general, owing to the less-ordered arrangement of the atoms at the GB plane usually associated with an excess volume, high-angle and high-energy GBs and random GBs are deemed to be more attractive for impurity segregation [1] than low-angle, low-energy, and symmetric tilt GBs. Based on Table 1, it can be seen that high-angle GB1 with the misorientation angle of 54.2° has the largest S excess of 56.3 ng/cm^2 S, whereas the S segregation at GB2 as a low-angle GB (only 3.6°) is 20.2 ng/cm^2. The Σ5 GB also has a low amount of S segregation (27.3 ng/cm^2). This result agrees very well with previous studies wherein it has been shown that P segregation in Fe–C alloy was three times higher for high-angle GBs rather than low-angle GBs [87]. Thus, it is reasonable to consider that the random NiS1 GB with high-angle misorientation has a higher amount of segregated S compared with the NiS2 as a symmetric Σ5 GB. As a result, the different structure of NiS1 compared with NiS2 can be the reason for a larger S excess for NiS1 and consequently for a more-pronounced embrittlement as is confirmed from the *L–D* curve and fractographic investigations.

4.3. Decohesion enhancement of the GB hosting S and H

Solute H can downturn the ductility and change the fracture mode from transgranular to IG. However, H-induced IG cracking needs a number of other factors such as sufficient H content and the stress condition. Co-segregation of S alongside H to the GB can consolidate their embrittling effect [88]. Accordingly, based on the experimental results on S-doped bi-crystals, in both NiS1 and NiS2 GBs, the crack nucleates from the GB, which demonstrates that the S segregation has a weakening effect on the GB strength. Adding H to the system by cathodic charging enhanced the embrittling effect by shifting the sudden load drop to approximately 2.5 and 1 μm displacement for NiS1 and NiS2 GBs, respectively. However, it is not clear whether the co-segregation of H and S has a synergistic effect on the

mechanical response of the material. For Fe it has been previously shown that the effect of S and H on the GB strength were independent and additive [89]. According to the DFT results in Fig. 11, the slope of the line related to W_{sep} for S (blue triangle line) is the same as for the case with 0.25 ML H present (black pentagon line). A similar trend can be observed for the effect of H on W_{sep} with and without 0.25 ML S (red circle and pink square lines, respectively). This result confirms the independent embrittling effect of the H and S.

On the other hand, it could be possible that the presence of S enhances the H ingress into the material owing to the detrimental effect of this impurity on the H recombination reaction [90, 91], a fact that is not yet considered in DFT calculations. Preventing the recombination reaction by S can increase the local adsorption and enrichment of H at the metal GBs. Likewise, this phenomenon is reported for the Sb and Sn segregated GBs in Ni, which are also recombination poisons [12]. It is suggested that H preferentially ingressed into the Ni specimens in the proximity of GB intersections with the free surface owing to the presence of Sb and Sn, which as H recombination poisons stimulate the absorption of H by the metal. Co-segregation of S and H has also been investigated by the molecular orbital model [92]. According to this work, forming a network of S–S bonds within the GB leads to an increase in the shear stress and simultaneously reduces the cohesive strength of the GB. However, they suggested that by forming a network of bonds with incorporation of a third element such as H, the shear strength will increase while, the cohesive strength of the GB will not be affected. However, this hypothesis is not fully in line with our results. As seen in Figs. 6 and 7, the shear bands are activated in all H-free conditions, even with the presence of a high amount of S in the GBs. In the case of S-doped NiS1 GB, which cracked in a fully brittle manner, the slip lines are still observable especially on the free-standing grain, which is more favorable for dislocation movements. Thus, it is hard to see any enhancement in shear stress for S-doped specimens. In contrast, adding H to the system was more effective at hindering the dislocation movements and fewer slip lines revealed on the surface even in the pure Ni sample. Hydrogen can pin the dislocations and, hence, increase the dislocation as depicted in Fig. 12.

According to Table 3, adding 0.25 ML of S decreased the work of separation by 9.19%, whereas 2.69% reduction has been calculated for the same amount of H at the GB. The same behavior of greater effect of S is also observed for co-segregation of the S and H in Fig. 11, by considering the slopes for increasing H and S, respectively. The steeper slope for increasing S shows the greater effect of S on GB decohesion.

The GB embrittling effect of H, S, and H+S can be interpreted by considering the competition between the brittle fracture and the dislocation emission, which is schematically shown in Fig. 12. In pure Ni, the energy needed for emitting dislocations is lower than the work of separation for the GB, therefore we observe activation of slip planes near the GB (Fig. 12(a)). Adding H to the system enhances the required energy for dislocation emission along with decreasing W_{sep}. The associated energy changes in the system are still not sufficient to induce IG cracking, although H already confines the plastic zone to the notch area (Fig. 12(b)). In the case of S segregation to the Ni GB, the work of separation decreases and becomes virtually equivalent to the value of the dislocation emission energy, which results in simultaneous GB decohesion and activation of slip planes near the GB (Fig. 12(c)). Co-segregation of H and S to the GB decreases the work of separation leading to IG cracking and possibly leads to an increase in the dislocation emission energy owing to dislocation pinning by H near the GB (Fig. 12(d)). It can be said that S is more influential on the decohesion reduction, whereas H is more effective on increasing the shear stress for plastic deformation. Subsequently, the co-segregation of S+H can have a double side brittleness effect on both decohesion and shear stress.

4.4. H concentration enhancement

As mentioned previously, the H concentration is one of the main parameters controlling the mechanical response of the material. Therefore, to investigate the effect of H concentration enhancement on the GB embrittlement, 0.002 M $Na_2S_2O_4$ as H recombination poison was added to the charging glycerol-based solution for testing beams containing NiS2 GB. Owing to the poison, the adsorbed and absorbed H concentration in the material increases [93].

Comparing *L–D* curves in Fig. 4 for NiS1 and NiS2 GBs in H-free condition, it can be inferred that the NiS2 GB shows more ductility compared with NiS1. However, for 2 h of H charging, the presence of poison for bending the beam containing NiS2 GB causes more ductility loss in comparison with NiS1, which is tested without any poison. As discussed in Section 4.2, the NiS2 GB possesses lower misorientation angle and probably a lower amount of S compared with NiS1 GB. Thus, NiS2 is less prone to cracking. However, the higher content of H obtained by adding poison into the solution, can overcome the structural and chemical effect in the way that the NiS2 GB fails easier and shows enhanced embrittlement compared with NiS1 with the same H-charging time but no poison. By

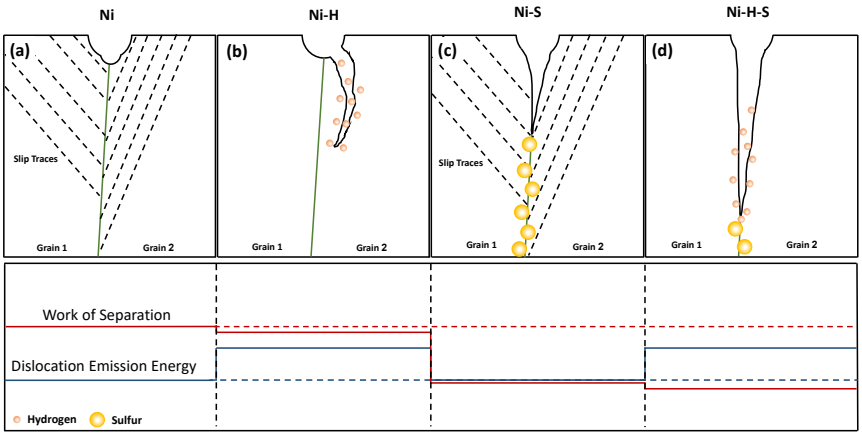

Figure 12: Schematic representation of the crack propagation for pure Ni, H-charged, S-doped, and Ni–S–H conditions with the corresponding work of separation and dislocation emission energy level.

accumulation of high amount of H, the atomic decohesion of the GB take place according to the HEDE mechanism which led to the observed GB opening. In accordance with our results, it is reported that by increasing the cathodic potential, which would enhance the H concentration in the Ni GB, the critical S concentration to cause 50 % IG fracture decreases [8, 20]. By applying −0.72 V (SCE) cathodic potential, the critical S segregation concentration drops to about ~2 at.%, whereas with a potential of −0.3V (SCE) the critical S segregation concentration was 6.5 at.%. In addition, Lassia and Birnbaum [79] reported a change from ductile fracture to a mixed brittleductile and complete IG fracture by increasing the H content from 0 at.ppm. to 60 and 600 at.ppm., respectively, for a specimen with a S concentration of 0.1 S/Ni.

Low diffusivity coupled with high solubility in Ni results in a high H concentration gradient near to the surface. This gradient may result in some structural effects close to the sample surface and accordingly a considerable change in the mechanical properties of the material. Changes in the flow stress of the H-charged Ni samples is one of these effects. As shown in Fig. 13, continuing the in situ testing in the poison-containing solution revealed a hardening effect for the beams tested after 3 h of charging. Although the sudden load drop for both 3 h and 2 h charged samples happens in the same displacement, for the 3 h charging condition the beam shows about 20% increase in the maximum tolerated load. After 3 h of charging in poisoned solution, in situ charging was stopped, the samples were taken out of the solution, rinsed with distilled water and later with ethanol, which was followed by storing them in a desiccator. Then, the beams were bent after 2, 4, and 17 h. For 2 h of being in air (H-charged 3 h + air 2 h), the same *L–D* curve as 3 h in situ charging is achieved. Giving further time to the sample in a H-free environment turns over the ductility of the tested beam up to 50% after 17 hours of being in air, whereas the observed hardening effect was persistent in all *L–D* curves obtained after 3 h of charging.

The observed increase in the maximum tolerated force can be interpreted as the hardening effect caused by H-dislocation interaction. Several researchers have reported the hardening effect during H-charging in both BCC [94] and FCC materials [71]. As an example, Kimura and Birnbaum [63] observed the hardening effect when they charged the Ni samples in a solution containing H recombination poison at a current density of 0.8 mA/cm^2. Their reported current density is in a comparable range to that used in our experiment. However, there is a significant difference in the obtained results. The hardening effect reported in their work was reversible and the flow stress turned back to that recorded in the absence of H, when the cathodic potential was removed. In contrast, the maximum tolerated load enhancement in the *L–D* curves shown in Fig. 13 was persistent and did not show any decrease even after 17 h of keeping the sample in air. Hence, it seems that there are other factors playing a role in the irreversible hardening effect observed when the H-charging was stopped.

The high H concentration gradient and subsequently stress gradient at the metal sub-surface can lead to formation of the localized hydride or H clusters at the dislocation cores [95, 96]. It is reported that these phases can lock the Frank–Read and other dislocation sources. Locking of the local dislocations formed at the dislocation core would lead to large dislocation pile ups resulting in surface hardening [97]. In addition, Kimura and Birnbaum showed that

the hardening effect caused by Ni hydride formation is irreversible even after aging for several hours [63]. Hydride is a brittle phase and acts as a barrier to dislocation motion. Despite the thermodynamically unstable nature of Ni–H at room temperature, it is documented that if high activity of H atoms is present, hydride formation would be possible [98]. During the out gassing, although the hydride layer reverts to Ni owing to its unstable nature at room temperature [63, 99], the remaining high surface dislocation density causes the residual increase in the flow curve [63].

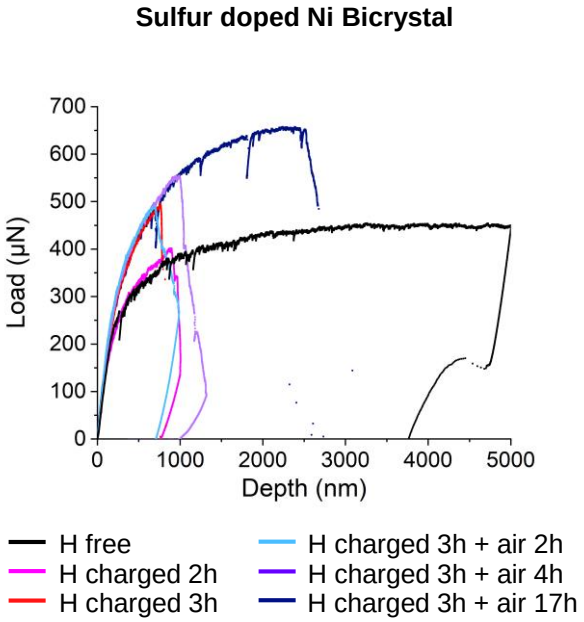

Figure 13: Load–displacement curves of the S-doped (GB NiS2 in Table 2) bi-crystal beams tested with H-free, in situ electrochemical H-charging, and post-charging in air conditions. The H-charging electrolyte contained 0.002 M $Na_2S_2O_4$ as the H recombination poison.

5. Conclusions

The current work has focused on a combined experimental and theoretical investigation of the effect of S and H segregation on the mechanical properties of selected GBs. In situ micro-cantilever bending tests have been utilized to investigate the mechanical response of the GBs, whereas DFT calculations have been used to study the interaction of S and H with the GB at the atomic level. Cantilever bending tests in pure Ni samples without S segregation result in a ductile behavior accompanied by slip traces on the surface. While testing pure Ni in H-charged condition, the crack is initiated from the notch area and fewer activated slip traces are observed. The observed difference is discussed by the impeding effect of the H on dislocation motions and localizing the plasticity to the crack tip. It is showed that the crack formed in the H-charged pure Ni beam is neither IG nor purely brittle. In this case, H concentration at the GB does not reach to the critical amount to cause IG atomic decohesion based on the HEDE mechanism. Segregation of S to GB leads to the IG cracking during the bending test. The crack reveals brittle type of fracture and propagates through the GB. Hydrogen-charging makes the IG fracture even more prominent and causes a sooner sudden drop in *L–D* curves compared with H-free conditions. Based on the DFT results, it is shown that the GB cohesion is much more reduced by S enrichment in comparison with H enrichment. Even though the co-segregation of S and H substantially reduces the cohesion of the selected GB, no interaction between S and H effects is obtained by DFT calculations.

Acknowledgment

The authors gratefully acknowledge the financial support under the scope of the COMET program within the K2 Center “Integrated Computational Material, Process and Product Engineering (IC-MPPE)” (Project No. 859480).

This program is supported by Voestalpine BÖHLER Edelstahl GmbH & Co KG, the Austrian Federal Ministries for Climate Action, Environment, Energy, Mobility, Innovation and Technology (BMK) and for Digital and Economic Affairs (BMDW), represented by the Austrian Research Funding Association (FFG), and the federal states of Styria, Upper Austria, and Tyrol. The computational results presented have been obtained using the Vienna Scientific Cluster (VSC). The Research Council of Norway is acknowledged for the support to the Norwegian Micro- and Nano-Fabrication Facility, NorFab (Project No. 245963/F50). The authors express their gratitude to Dr. Mohammad Zamanzade for his constructive comments and discussion. Sondre Fossheim is also acknowledged for his contribution to producing the micro-samples.

Data availability

The raw/processed data required to reproduce these findings cannot be shared at this time as the data also forms part of an ongoing study.

References

[1] P. Lejček, Grain Boundary Segregation in Metals, Springer Berlin Heidelberg, Berlin, 2010.

[2] P. Lejček, M. Šob, V. Paidar, Interfacial segregation and grain boundary embrittlement: An overview and critical assessment of experimental data and calculated results, Prog. Mater. Sci. 87 (2017) 83–139. doi:https://doi.org/10.1016/j.pmatsci.2016.11.001.
URL http://www.sciencedirect.com/science/article/pii/S0079642516300755

[3] J. R. Rice, J.-S. Wang, Embrittlement of interfaces by solute segregation, Mater. Sci. Eng. A 107 (1989) 23 – 40. doi:https://doi.org/10.1016/0921-5093(89)90372-9.
URL http://www.sciencedirect.com/science/article/pii/0921509389903729

[4] S. Lynch, A review of underlying reasons for intergranular cracking for a variety of failure modes and materials and examples of case histories, Engineering Failure Analysis 100 (2019) 329–350. doi:https://doi.org/10.1016/j.engfailanal.2019.02.027.

[5] S. Mahalingam, P. E. J. Flewitt, J. F. Knott, The ductilebrittle transition for nominally pure polycrystalline nickel, Mater. Sci. Eng.: A 564 (2013) 342–350. doi:https://doi.org/10.1016/j.msea.2012.11.106.
URL http://www.sciencedirect.com/science/article/pii/S0921509312016589

[6] M. Lozinsky, G. Volkogon, N. Pertsovsky, Investigation of the influence of zirconium additions on the ductility and deformation structure of nickel over a wide temperature range, Russ. Metall. 5 (1967) 65–72.

[7] A. Larere, M. Guttmann, P. Dumoulin, C. Roques-Carmes, Auger electron spectroscopy study of the kinetics of intergranular and surface segregations in nickel during annealing, Acta Metall. 30 (3) (1982) 685–693.

[8] S. M. Bruemmer, R. H. Jones, M. T. Thomas, D. R. Baer, Influence of sulfur, phosphorus, and antimony segregation on the intergranular hydrogen embrittlement of nickel, Metall. Trans. A 14 (1) (1983) 223–232. doi:10.1007/bf02651619.
URL http://dx.doi.org/10.1007/BF02651619

[9] W. T. Geng, A. J. Freeman, R. Wu, C. B. Geller, J. E. Raynolds, Embrittling and strengthening effects of hydrogen, boron, and phosphorus on a $\sigma 5$ nickel grain boundary, Phys. Rev. B 60 (1999) 7149–7155. doi:10.1103/PhysRevB.60.7149.
URL https://link.aps.org/doi/10.1103/PhysRevB.60.7149

[10] V. Razumovskiy, A. Lozovoi, I. Razumovskii, First-principles-aided design of a new Ni-base superalloy: Influence of transition metal alloying elements on grain boundary and bulk cohesion, Acta Mater. 82 (Supplement C) (2015) 369 – 377. doi:https://doi.org/10.1016/j.actamat.2014.08.047.
URL http://www.sciencedirect.com/science/article/pii/S1359645414006612

[11] R. H. Jones, S. M. Bruemmer, M. T. Thomas, D. R. Baer, Hydrogen pressure dependence of the fracture mode transition in nickel, Metall. Trans. A 14 (8) (1983) 1729–1736. doi:10.1007/bf02654401.
URL http://dx.doi.org/10.1007/BF02654401

[12] R. M. Latanision, H. Opperhauser, The intergranular embrittlement of nickel by hydrogen: The effect of grain boundary segregation, Metall. Trans. 5 (2) (1974) 483–492. doi:10.1007/BF02644118.
URL https://doi.org/10.1007/BF02644118

[13] K. M. Bertsch, S. Wang, A. Nagao, I. M. Robertson, Hydrogen-induced compatibility constraints across grain boundaries drive intergranular failure of ni, Mater. Sci. Eng. A 760 (2019) 58–67. doi:https://doi.org/10.1016/j.msea.2019.05.036.
URL http://www.sciencedirect.com/science/article/pii/S092150931930658

[14] H. Vehoff, W. Rothe, Gaseous hydrogen embrittlement in fesi-and ni-single crystals, in: Perspectives in Hydrogen in Metals, Elsevier, 1986, pp. 647–659.

[15] M. B. Djukic, G. M. Bakic, V. Sijacki Zeravcic, A. Sedmak, B. Rajicic, The synergistic action and interplay of hydrogen embrittlement mechanisms in steels and iron: Localized plasticity and decohesion, Engineering Fracture Mechanics 216 (2019) 106528. doi:https://doi.org/10.1016/j.engfracmech.2019.106528.

[16] M. L. Martin, M. Dadfarnia, A. Nagao, S. Wang, P. Sofronis, Enumeration of the hydrogen-enhanced localized plasticity mechanism for hydrogen embrittlement in structural materials, Acta Materialiadoi:https://doi.org/10.1016/j.actamat.2018.12.014.

[17] R. Kirchheim, Solid solution softening and hardening by mobile solute atoms with special focus on hydrogen, Scripta Materialia 67 (9) (2012) 767–770. doi:10.1016/j.scriptamat.2012.07.022.

[18] M. L. Martin, B. P. Somerday, R. O. Ritchie, P. Sofronis, I. M. Robertson, Hydrogen-induced intergranular failure in nickel revisited, Acta Materialia 60 (6) (2012) 2739–2745. doi:http://dx.doi.org/10.1016/j.actamat.2012.01.040.

[19] A. Metsue, A. Oudriss, X. Feaugas, Hydrogen solubility and vacancy concentration in nickel single crystals at thermal equilibrium: New insights from statistical mechanics and *ab initio* calculations, J. Alloys Compd. 656 (2016) 555–567. doi:10.1016/j.jallcom.2015.09.252.
URL http://www.sciencedirect.com/science/article/pii/S0925838815312299

[20] J. K. Heuer, P. R. Okamoto, N. Q. Lam, J. F. Stubbins, Relationship between segregation-induced intergranular fracture and melting in the nickel sulfur system, Applied Physics Letters 76 (23) (2000) 3403–3405. arXiv:https://doi.org/10.1063/1.126660, doi:10.1063/1.126660.
URL https://doi.org/10.1063/1.126660

[21] H. Vehoff, C. Laird, D. Duquette, The effects of hydrogen and segregation on fatigue crack nucleation at defined grain boundaries in nickel bicrystals, Acta Metall. 35 (12) (1987) 2877 – 2886. doi:https://doi.org/10.1016/0001-6160(87)90286-0.
URL http://www.sciencedirect.com/science/article/pii/0001616087902860

[22] D. Di Maio, S. Roberts, Measuring fracture toughness of coatings using focused-ion-beam-machined microbeams, J. Mater. Res. 20 (2) (2005) 299302. doi:10.1557/JMR.2005.0048.

[23] J. Ast, M. Ghidelli, K. Durst, M. Gken, M. Sebastiani, A. M. Korsunsky, A review of experimental approaches to fracture toughness evaluation at the micro-scale, Mater. Des. 173 (2019) 107762. doi:https://doi.org/10.1016/j.matdes.2019.107762.
URL http://www.sciencedirect.com/science/article/pii/S0264127519301996

[24] H. Dugdale, D. E. J. Armstrong, E. Tarleton, S. G. Roberts, S. Lozano-Perez, How oxidized grain boundaries fail, Acta Mater. 61 (13) (2013) 4707–4713. doi:http://dx.doi.org/10.1016/j.actamat.2013.05.012.
URL http://www.sciencedirect.com/science/article/pii/S1359645413003800

[25] A. Stratulat, D. E. J. Armstrong, S. G. Roberts, Micro-mechanical measurement of fracture behaviour of individual grain boundaries in ni alloy 600 exposed to a pressurized water reactor environment, Corros. Sci. 104 (2016) 9–16. doi:http://dx.doi.org/10.1016/j.corsci.2015.10.019.
URL http://www.sciencedirect.com/science/article/pii/S0010938X15301189

[26] M. Yamaguchi, M. Shiga, H. Kaburaki, Energetics of segregation and embrittling potency for non-transition elements in the ni Σ 5 (012) symmetrical tilt grain boundary: a first-principles study, J. Phys.: Condens. Matter 16 (23) (2004) 3933. doi:https://doi.org/10.1088/0953-8984/16/23/013.
URL http://stacks.iop.org/0953-8984/16/i=23/a=013

[27] M. Yamaguchi, M. Shiga, H. Kaburaki, First-principles study on segregation energy and embrittling potency of hydrogen in ni Σ 5(012) tilt grain boundary, J. Phys. Soc. Jpn. 73 (2) (2004) 441–449. doi:https://doi.org/10.1143/JPSJ.73.441.
URL https://doi.org/10.1143/JPSJ.73.441

[28] D. D. Stefano, M. Mrovec, C. Elssser, First-principles investigation of hydrogen trapping and diffusion at grain boundaries in nickel, Acta Mater. 98 (2015) 306 – 312. doi:https://doi.org/10.1016/j.actamat.2015.07.031.
URL http://www.sciencedirect.com/science/article/pii/S1359645415005029

[29] S. He, W. Ecker, R. Pippan, V. I. Razumovskiy, Hydrogen-enhanced decohesion mechanism of the special Σ5(012)[100] grain boundary in ni with mo and c solutes, Comput. Mater. Sci. 167 (2019) 100 – 110. doi:https://doi.org/10.1016/j.commatsci.2019.05.029.
URL http://www.sciencedirect.com/science/article/pii/S0927025619303076

[30] T. Depover, K. Verbeken, Evaluation of the effect of v4c3 precipitates on the hydrogen induced mechanical degradation in fe-c-v alloys, Materials Science and Engineering: A 675 (2016) 299 – 313. doi:https://doi.org/10.1016/j.msea.2016.08.053.
URL http://www.sciencedirect.com/science/article/pii/S0921509316309662

[31] T. Depover, K. Verbeken, Hydrogen trapping and hydrogen induced mechanical degradation in lab cast fe-c-cr alloys, Materials Science and Engineering: A 669 (2016) 134 – 149. doi:https://doi.org/10.1016/j.msea.2016.05.018.
URL http://www.sciencedirect.com/science/article/pii/S0921509316305111

[32] B. He, W. Xiao, W. Hao, Z. Tian, First-principles investigation into the effect of cr on the segregation of multi-H at the Fe Σ 3 (111) grain boundary, J. Nucl. Mater. 441 (1) (2013) 301 – 305. doi:https://doi.org/10.1016/j.jnucmat.2013.06.015.
URL http://www.sciencedirect.com/science/article/pii/S0022311513008386

[33] M. Yuasa, M. Hakamada, Y. Chino, M. Mabuchi, First-principles study of hydrogen-induced embrittlement in Fe grain boundary with Cr segregation, ISIJ Int. 55 (5) (2015) 1131–1134. doi:10.2355/isijinternational.55.1131.
URL https://www.jstage.jst.go.jp/article/isijinternational/55/5/55_1131/_pdf/-char/ja

[34] D. A. Aksyonov, T. Hickel, J. Neugebauer, A. G. Lipnitskii, The impact of carbon and oxygen in alpha-titanium:ab initiostudy of solution enthalpies and grain boundary segregation, J. Phys.: Condens. Matter. 28 (38) (2016) 385001. doi:10.1088/0953-8984/28/38/385001.
URL https://doi.org/10.1088%2F0953-8984%2F28%2F38%2F385001

[35] D. Scheiber, L. Romaner, R. Pippan, P. Puschnig, Impact of solute-solute interactions on grain boundary segregation and cohesion in molybdenum, Phys. Rev. Mater. 2 (2018) 093609. doi:10.1103/PhysRevMaterials.2.093609.
URL https://link.aps.org/doi/10.1103/PhysRevMaterials.2.093609

[36] M. Yamaguchi, M. Shiga, H. Kaburaki, Grain boundary decohesion by impurity segregation in a nickel-sulfur system, Science 307 (5708) (2005) 393–397. arXiv:https://science.sciencemag.org/content/307/5708/393.full.pdf, doi:10.1126/science.1104624.
URL https://science.sciencemag.org/content/307/5708/393

[37] M. Yamaguchi, M. Shiga, H. Kaburaki, Response to comment on "grain boundary decohesion by impurity segregation in a nickel-sulfur system", Science 309 (5741) (2005) 1677–1677. arXiv:https://science.sciencemag.org/content/309/5741/1677.4.full.pdf, doi:10.1126/science.1112218.
URL https://science.sciencemag.org/content/309/5741/1677.4

[38] W. T. Geng, J.-S. Wang, G. B. Olson, Comment on "grain boundary decohesion by impurity segregation in a nickel-sulfur system", Science

309 (5741) (2005) 1677–1677. arXiv:https://science.sciencemag.org/content/309/5741/1677.3.full.pdf, doi:10.1126/science.1112072.
URL https://science.sciencemag.org/content/309/5741/1677.3
[39] G. Schusteritsch, E. Kaxiras, Sulfur-induced embrittlement of nickel: a first-principles study, Modell. Simul. Mater. Sci. Eng. 20 (6) (2012) 065007. doi:10.1088/0965-0393/20/6/065007.
URL https://doi.org/10.1088%2F0965-0393%2F20%2F6%2F065007
[40] J. R. Rice, R. Thomson, Ductile versus brittle behaviour of crystals, Philos. Mag. A 29 (1) (1974) 73–97. doi:10.1080/14786437408213555.
URL https://doi.org/10.1080/14786437408213555
[41] D. McLean, Grain Boundaries in Metals, Clarendon Press, Oxford, 1957.
[42] D. Scheiber, L. Romaner, F. Fischer, J. Svoboda, Kinetics of grain boundary segregation in multicomponent systems The example of a Mo-C-B-O system, Scr. Mater. 150 (2018) 110–114. doi:10.1016/j.scriptamat.2018.03.011.
URL http://linkinghub.elsevier.com/retrieve/pii/S1359646218301635
[43] D. Scheiber, T. Jechtl, J. Svoboda, F. Fischer, L. Romaner, On solute depletion zones along grain boundaries during segregation, Acta Mater.doi:https://doi.org/10.1016/j.actamat.2019.10.040.
URL http://www.sciencedirect.com/science/article/pii/S1359645419307025
[44] N. Kheradmand, H. Vehoff, A. Barnoush, An insight into the role of the grain boundary in plastic deformation by means of a bicrystalline pillar compression test and atomistic simulation, Acta Mater. 61 (19) (2013) 7454–7465.
[45] F. Christien, P. Risch, Cross-sectional measurement of grain boundary segregation using wds, Ultramicroscopy 170 (2016) 107 – 112.
[46] A. Barnoush, H. Vehoff, Recent developments in the study of hydrogen embrittlement: Hydrogen effect on dislocation nucleation, Acta Mater. 58 (16) (2010) 5274 – 5285.
[47] A. Barnoush, H. Vehoff, In situ electrochemical nanoindentation: A technique for local examination of hydrogen embrittlement, Corros. Sci. 50 (1) (2008) 259 – 267. doi:https://doi.org/10.1016/j.corsci.2007.05.026.
URL http://www.sciencedirect.com/science/article/pii/S0010938X07001655
[48] T. Hajilou, Y. Deng, B. R. Rogne, N. Kheradmand, A. Barnoush, In situ electrochemical microcantilever bending test: A new insight into hydrogen enhanced cracking, Scr. Mater. 132 (2017) 17 – 21. doi:https://doi.org/10.1016/j.scriptamat.2017.01.019.
URL http://www.sciencedirect.com/science/article/pii/S1359646217300295
[49] T. Hajilou, M. S. Hope, A. H. Zavieh, N. Kheradmand, R. Johnsen, A. Barnoush, In situ small-scale hydrogen embrittlement testing made easy: An electrolyte for preserving surface integrity at nano-scale during hydrogen charging, Int. J. Hydrog. Energy 43 (27) (2018) 12516 – 12529. doi:https://doi.org/10.1016/j.ijhydene.2018.04.168.
URL http://www.sciencedirect.com/science/article/pii/S0360319918313570
[50] P. E. Blöchl, Projector augmented-wave method, Phys. Rev. B 50 (24) (1994) 17953. doi:10.1103/PhysRevB.50.17953.
URL https://link.aps.org/doi/10.1103/PhysRevB.50.17953
[51] G. Kresse, D. Joubert, From ultrasoft pseudopotentials to the projector augmented-wave method, Phys. Rev. B 59 (3) (1999) 1758. doi:10.1103/PhysRevB.59.1758.
URL https://link.aps.org/doi/10.1103/PhysRevB.59.1758
[52] G. Kresse, J. Hafner, *Ab initio* molecular dynamics for open-shell transition metals, Phys. Rev. B 48 (1993) 13115–13118. doi:10.1103/PhysRevB.48.13115.
URL http://link.aps.org/doi/10.1103/PhysRevB.48.13115
[53] G. Kresse, J. Furthmüller, Efficiency of ab-initio total energy calculations for metals and semiconductors using a plane-wave basis set, Comput. Mater. Sci. 6 (1) (1996) 15 – 50. doi:http://dx.doi.org/10.1016/0927-0256(96)00008-0.
URL http://www.sciencedirect.com/science/article/pii/0927025696000080
[54] J. P. Perdew, K. Burke, M. Ernzerhof, Generalized gradient approximation made simple, Phys. Rev. Lett. 77 (1996) 3865–3868. doi:10.1103/PhysRevLett.77.3865.
URL https://link.aps.org/doi/10.1103/PhysRevLett.77.3865
[55] H. J. Monkhorst, J. D. Pack, Special points for brillouin-zone integrations, Phys. Rev. B 13 (1976) 5188–5192. doi:10.1103/PhysRevB.13.5188.
URL https://link.aps.org/doi/10.1103/PhysRevB.13.5188
[56] D. Kandaskalov, D. Monceau, C. Mijoule, D. Conntable, First-principles study of sulfur multi-absorption in nickel and its segregation to the ni(100) and ni(111) surfaces, Surf. Sci. 617 (2013) 15 – 21. doi:https://doi.org/10.1016/j.susc.2013.06.019.
URL http://www.sciencedirect.com/science/article/pii/S003960281300191X
[57] D. Connétable, É. Andrieu, D. Monceau, First-principles nickel database: Energetics of impurities and defects, Comput. Mater. Sci. 101 (2015) 77–87. doi:http://dx.doi.org/10.1016/j.commatsci.2015.01.017.
[58] R. Nazarov, T. Hickel, J. Neugebauer, Ab initio study of H-vacancy interactions in fcc metals: Implications for the formation of superabundant vacancies, Phys. Rev. B 89 (14) (2014) 144108. doi:10.1103/PhysRevB.89.144108.
URL https://link.aps.org/doi/10.1103/PhysRevB.89.144108
[59] L. Wang, H. Bei, T. Li, Y. Gao, E. George, T. Nieh, Determining the activation energies and slip systems for dislocation nucleation in body-centered cubic mo and face-centered cubic ni single crystals, Scr. Mater. 65 (3) (2011) 179 – 182. doi:https://doi.org/10.1016/j.scriptamat.2011.03.036.
URL http://www.sciencedirect.com/science/article/pii/S1359646211001680
[60] A. P. Sutton, R. W. Balluffi, A. Sutton, Interfaces in crystalline materials, Clarendon Press Oxford, 1995.
[61] D. Scheiber, R. Pippan, P. Puschnig, L. Romaner, Ab initio calculations of grain boundaries in bcc metals, Model. Simul. Mater. Sci. Eng. 24 (3) (2016) 035013. doi:10.1088/0965-0393/24/3/035013.
URL https://doi.org/10.1088%2F0965-0393%2F24%2F3%2F035013
[62] A. Pineau, A. Benzerga, T. Pardoen, Failure of metals i: Brittle and ductile fracture, Acta Mater. 107 (2016) 424 – 483. doi:https:

//doi.org/10.1016/j.actamat.2015.12.034.
URL http://www.sciencedirect.com/science/article/pii/S1359645415301403
[63] A. Kimura, H. Birnbaum, The effects of cathodically charged hydrogen on the flow stress of nickel and nickel-carbon alloys, Acta Metall. 35 (5) (1987) 1077–1088.
[64] M. Yamaguchi, M. Shiga, H. Kaburaki, Grain boundary decohesion by sulfur segregation in ferromagnetic iron and nickel - a first-principles study, Mater. Trans. 47 (11) (2006) 2682–2689. doi:10.2320/matertrans.47.2682.
[65] A. Winkler, K. D. Rendulic, Measurements of bulk concentration in the ppm-Region by means of surface segregation: The System Sulphur-Nickel, in: M. Grasserbauer, M. K. Zacherl (Eds.), Zehntes Kolloquium über metallkundliche Analyse, Springer Vienna, Vienna, 1981, pp. 321–327.
[66] A. Alvaro, I. T. Jensen, N. Kheradmand, O. Lvvik, V. Olden, Hydrogen embrittlement in nickel, visited by first principles modeling, cohesive zone simulation and nanomechanical testing, Int. J. Hydrog. Energy 40 (47) (2015) 16892 – 16900, special issue on 1st International Conference on Hydrogen Storage, Embrittlement and Applications (Hy-SEA 2014), 26-30 October 2014, Rio de Janeiro, Brazil. doi:https://doi.org/10.1016/j.ijhydene.2015.06.069.
URL http://www.sciencedirect.com/science/article/pii/S0360319915015542
[67] I. J. T. Jensen, V. Olden, O. M. Løvvik, Decohesion energy of σ5(012)grain boundaries in ni as function of hydrogen content, Metall. Mater. Trans. A 50 (1) (2019) 451–456. doi:10.1007/s11661-018-4982-8.
URL https://doi.org/10.1007/s11661-018-4982-8
[68] M. Allart, F. Christien, R. L. Gall, P. Nowakowski, C. Grovenor, A multi-technique investigation of sulfur grain boundary segregation in nickel, Scr. Mater. 68 (10) (2013) 793 – 796. doi:https://doi.org/10.1016/j.scriptamat.2013.01.028.
URL http://www.sciencedirect.com/science/article/pii/S135964621300050X
[69] H. Mehrer, N. Stolica, Diffusion in Solid Metals and Alloys, Vol. 26 of Landolt-Börnstein - Group III Condensed Matter, Springer-Verlag, Berlin/Heidelberg, 1990. doi:10.1007/b37801.
URL http://materials.springer.com/bp/docs/978-3-540-46109-8
[70] M. Hill, E. Johnson, The diffusivity of hydrogen in nickel, Acta Metall. 3 (6) (1955) 566–571. doi:10.1016/0001-6160(55)90116-4.
URL https://www.sciencedirect.com/science/article/pii/0001616055901164
[71] J. Kacher, B. P. Eftink, B. Cui, I. M. Robertson, Dislocation interactions with grain boundaries, Current Opinion in Solid State and Materials Science 18 (4) (2014) 227–243. doi:http://dx.doi.org/10.1016/j.cossms.2014.05.004.
URL http://www.sciencedirect.com/science/article/pii/S1359028614000217http://ac.els-cdn.com/S1359028614000217/1-s2.0-S1359028614000217-main.pdf?_tid=2ce37376-bdfc-11e5-984e-00000aacb362&acdnat=1453132828_ba5498edb0319e0341917ce59a77bac1
[72] B. R. S. Rogne, N. Kheradmand, Y. Deng, A. Barnoush, In situ micromechanical testing in environmental scanning electron microscope: A new insight into hydrogen-assisted cracking, Acta Mater. 144 (2018) 257–268.
[73] Y. Ogawa, D. Birenis, H. Matsunaga, A. Thgersen, y. Prytz, O. Takakuwa, J. Yamabe, Multi-scale observation of hydrogen-induced, localized plastic deformation in fatigue-crack propagation in a pure iron, Scripta Materialia 140 (2017) 13–17. doi:http://dx.doi.org/10.1016/j.scriptamat.2017.06.037.
[74] Y. Deng, A. Barnoush, Hydrogen embrittlement revealed via novel in situ fracture experiments using notched micro-cantilever specimens, Acta Mater. 142 (2018) 236 – 247. doi:https://doi.org/10.1016/j.actamat.2017.09.057.
URL http://www.sciencedirect.com/science/article/pii/S1359645417308273
[75] D. Wan, Y. Deng, J. I. H. Meling, A. Alvaro, A. Barnoush, Hydrogen-enhanced fatigue crack growth in a single-edge notched tensile specimen under in-situ hydrogen charging inside an environmental scanning electron microscope, Acta Mater. 170 (2019) 87 – 99. doi:https://doi.org/10.1016/j.actamat.2019.03.032.
URL http://www.sciencedirect.com/science/article/pii/S1359645419301752
[76] H. Vehoff, P. Neumann, Crack propagation and cleavage initiation in fe-2.6%-si single crystals under controlled plastic crack tip opening rate in various gaseous environments, Acta Metall. 28 (3) (1980) 265–272. doi:https://doi.org/10.1016/0001-6160(80)90161-3.
[77] S. Pu, S. Ooi, Hydrogen transport by dislocation movement in austenitic steel, Mater. Sci. Eng. A (2019) 138059.
[78] C. McMahon Jr, Hydrogen-induced intergranular fracture of steels, Eng. Fract. Mech. 68 (6) (2001) 773–788.
[79] D. Lassila, H. Birnbaum, The effect of diffusive hydrogen segregation on fracture of polycrystalline nickel, Acta Metall. 34 (7) (1986) 1237–1243.
[80] A. Oudriss, J. Creus, J. Bouhattate, E. Conforto, C. Berziou, C. Savall, X. Feaugas, Grain size and grain-boundary effects on diffusion and trapping of hydrogen in pure nickel, Acta Mater. 60 (19) (2012) 6814–6828.
[81] M. Zamanzade, C. Müller, J. R. Velayarce, C. Motz, Susceptibility of different crystal orientations and grain boundaries of polycrystalline ni to hydrogen blister formation, Int. J. Hydrog. Energy 44 (14) (2019) 7706–7714.
[82] A. Tehranchi, W. Curtin, Atomistic study of hydrogen embrittlement of grain boundaries in nickel: I. fracture, J. Mech. Phys. Solids 101 (2017) 150–165.
[83] R. Messmer, C. Briant, The role of chemical bonding in grain boundary embrittlement, Acta Metall. 30 (2) (1982) 457–467.
[84] M. Yamaguchi, M. Shiga, H. Kaburaki, Grain boundary decohesion by impurity segregation in a nickel-sulfur system, Science 307 (5708) (2005) 393–397.
[85] T. Watanabe, The impact of grain boundary character distribution on fracture in polycrystals, Mater. Sci. Eng. A 176 (1-2) (1994) 39–49.
[86] S. Tsurekawa, T. Tanaka, H. Yoshinaga, Grain boundary structure, energy and strength in molybdenum, Mater. Sci. Eng. A 176 (1-2) (1994) 341–348.
[87] A. Akhatova, F. Christien, V. Barnier, B. Radiguet, E. Cadel, F. Cuvilly, P. Pareige, Investigation of the dependence of phosphorus segregation on grain boundary structure in fe-p-c alloy: ross comparison between atom probe tomography and auger electron spectroscopy, Appl. Surf. Sci. 463 (2019) 203–210.
[88] D. H. Lassila, H. K. Birnbaum, Intergranular fracture of nickel: the effect of hydrogen-sulfur co-segregation, Acta Metall. 35 (7) (1987) 1815–1822. doi:http://dx.doi.org/10.1016/0001-6160(87)90127-1.

URL http://www.sciencedirect.com/science/article/pii/0001616087901271

[89] K. Shin, M. Meshii, Effect of sulfur segregation and hydrogen charging on intergranular fracture of iron, in: Perspectives in Hydrogen in Metals, Elsevier, 1986, pp. 693–700.

[90] H. Jarmolowicz, M. Smialowski, Effect of catalytic poisons on the production of nickel hydride by electrolytic charging of nickel with hydrogen, J. Catal. 1 (2) (1962) 165–170.

[91] M. Abd Elhamid, B. Ateya, K. Weil, H. Pickering, Effect of thiosulfate and sulfite on the permeation rate of hydrogen through iron, Corrosion 57 (5) (2001) 428–432.

[92] M. Eberhart, K. Johnson, R. Latanision, A molecular orbital model of intergranular embrittlement, Acta Metall. 32 (6) (1984) 955–959.

[93] M. A. Kappes, Evaluation of thiosulfate as a substitute for hydrogen sulfide in sour corrosion fatigue studies, Ph.D. thesis, The Ohio State University (2011).

[94] S. Asano, R. Otsuka, The lattice hardening due to dissolved hydrogen in iron and steel, Scr. Metall. 10 (11) (1976) 1015–1020.

[95] D. P. Abraham, C. J. Altstetter, The effect of hydrogen on the yield and flow stress of an austenitic stainless steel, Metallurgical and Materials transactions A 26 (11) (1995) 2849–2858.

[96] H. K. Birnbaum, P. Sofronis, Hydrogen-enhanced localized plasticitya mechanism for hydrogen-related fracture, Materials Science and Engineering: A 176 (1-2) (1994) 191–202.

[97] D. Ulmer, C. Altstetter, Hydrogen-induced strain localization and failure of austenitic stainless steels at high hydrogen concentrations, Acta Metallurgica et Materialia 39 (6) (1991) 1237–1248.

[98] E. Wollan, J. Cable, W. Koehler, The hydrogen atom positions in face centered cubic nickel hydride, J. Phys. Chem. Solids 24 (9) (1963) 1141–1143.

[99] E. Lunarska-Borowiecka, N. F. Fiore, Hydride formation in a ni-base superalloy, Metall. Trans. A 12 (1) (1981) 101–107.